The Pristine survey XIV: chemical analysis of two ultra-metal-poor stars

C. Lardo, L. Mashonkina, P. Jablonka, P. Bonifacio, E. Caffau, D. S. Aguado, J. I. González Hernández, F. Sestito, C. L. Kielty, K. A. Venn, et al.

To cite this version:

C. Lardo, L. Mashonkina, P. Jablonka, P. Bonifacio, E. Caffau, et al.. The Pristine survey XIV: chemical analysis of two ultra-metal-poor stars. Monthly Notices of the Royal Astronomical Society, 2021, 508 (2), pp.3068-3083. 10.1093/mnras/stab2847 . obspm-03364468

HAL Id: obspm-03364468

https://hal-obspm.ccsd.cnrs.fr/obspm-03364468v1

Submitted on 21 Apr 2023

Monthly Notices
of the
ROYAL ASTRONOMICAL SOCIETY

MNRAS **508,** 3068–3083 (2021)
Advance Access publication 2021 October 5
https://doi.org/10.1093/mnras/stab2847

The Pristine survey – XIV. Chemical analysis of two ultra-metal-poor stars

C. Lardo,[1]★ L. Mashonkina,[2] P. Jablonka,[3,4] P. Bonifacio,[4] E. Caffau,[4] D. S. Aguado,[5]
J. I. González Hernández,[6,7] F. Sestito,[8] C. L. Kielty,[8] K. A. Venn,[8] V. Hill,[9] E. Starkenburg,[10]
N. F. Martin,[11,12] T. Sitnova,[2] A. Arentsen,[11] R. G. Carlberg,[13] J. F. Navarro[8] and G. Kordopatis[9]

[1] *Dipartimento di Fisica e Astronomia, Università degli Studi di Bologna, Via Gobetti 93/2, I-40129 Bologna, Italy*
[2] *Institute of Astronomy, Russian Academy of Sciences, RU-119017 Moscow, Russia*
[3] *Laboratoire d'astrophysique, École Polytechnique Fédérale de Lausanne (EPFL), Observatoire, CH-1290 Versoix, Switzerland*
[4] *GEPI, Observatoire de Paris, Université PSL, CNRS, 5 Place Jules Janssen, F-92190 Meudon, France*
[5] *Institute of Astronomy, University of Cambridge, Madingley Road, Cambridge CB3 0HA, UK*
[6] *Instituto de Astrofísica de Canarias, Vía Láctea, E-38205 La Laguna, Tenerife, Spain*
[7] *Universidad de La Laguna, Departamento de Astrofísica, E- 38206 La Laguna, Tenerife, Spain*
[8] *Department of Physics and Astronomy, University of Victoria, Victoria, BC V8W 3P2, Canada*
[9] *Laboratoire Lagrange, Université de Nice Sophia-Antipolis, Observatoire de la Côte d'Azur, F-06300 Nice, France*
[10] *Kapteyn Astronomical Institute, University of Groningen, Landleven 12, NL-9747 AD Groningen, the Netherlands*
[11] *Université de Strasbourg, CNRS, Observatoire astronomique de Strasbourg, UMR 7550, F-67000 Strasbourg, France*
[12] *Max-Planck-Institut für Astronomie, K"onigstuhl 17, D-69117 Heidelberg, Germany*
[13] *Department of Astronomy and Astrophysics, University of Toronto, Toronto, ON M5S 3H4, Canada*

Accepted 2021 September 29. Received 2021 September 29; in original form 2021 June 21

ABSTRACT

Elemental abundances of the most metal-poor stars reflect the conditions in the early Galaxy and the properties of the first stars. We present a spectroscopic follow-up of two ultra-metal-poor stars ([Fe/H] < -4.0) identified by the survey *Pristine*: Pristine 221.8781+9.7844 and Pristine 237.8588+12.5660 (hereafter Pr 221 and Pr 237, respectively). Combining data with earlier observations, we find a radial velocity of -149.25 ± 0.27 and -3.18 ± 0.19 km s^{-1} for Pr 221 and Pr 237, respectively, with no evidence of variability between 2018 and 2020. From a one-dimensional (1D) local thermodynamic equilibrium (LTE) analysis, we measure $[\mathrm{Fe/H}]_{\mathrm{LTE}} = -4.79 \pm 0.14$ for Pr 221 and -4.22 ± 0.12 for Pr 237, in good agreement with previous studies. Abundances of Li, Na, Mg, Al, Si, Ca, Ti, Fe, and Sr were derived based on the non-LTE (NLTE) line formation calculations. When NLTE effects are included, we measure slightly higher metallicities: $[\mathrm{Fe/H}]_{\mathrm{NLTE}} = -4.40 \pm 0.13$ and -3.93 ± 0.12, for Pr 221 and Pr 237, respectively. Analysis of the *G* band yields $[\mathrm{C/Fe}]_{\mathrm{1D\text{-}LTE}} \leq +2.3$ and $[\mathrm{C/Fe}]_{\mathrm{1D\text{-}LTE}} \leq +2.0$ for Pr 221 and Pr 237. Both stars belong to the low-carbon band. Upper limits on nitrogen abundances are also derived. Abundances for other elements exhibit good agreement with those of stars with similar parameters. Finally, to get insight into the properties of their progenitors, we compare NLTE abundances to theoretical yields of zero-metallicity supernovae (SNe). This suggests that the SNe progenitors had masses ranging from 10.6 to 14.4 $\mathrm{M}_{\odot}$ and low-energy explosions with (0.3–1.2) $\times 10^{51}$ erg.

Key words: stars: abundances – Galaxy: abundances – Galaxy: evolution – Galaxy: formation – Galaxy: halo.

1 INTRODUCTION

The most metal-poor stars in the Galaxy tell us about the conditions found during the first stages of chemical enrichment (e.g. Beers & Christlieb 2005; Frebel & Norris 2015). Given their low metallicities, they are considered to be second-generation objects from the early Universe. Thus, their abundance patterns should reflect the properties of the first massive Population III (Pop III) stars.

Although much effort has been put on the study of this key stellar population over the past 50 yr, observations of the most metal-poor stars populating the Milky Way (MW) and its close satellites are relatively scarce. Indeed, the numbers of known extremely, ultra-, and hyper-metal-poor stars (stars with [Fe/H] < -3.0, [Fe/H] < -4.0, and [Fe/H] < -5.0; Beers & Christlieb 2005) are still exceedingly small (e.g. see the compilation presented in Sestito et al. 2019) and fewer than 20 stars are known to have iron abundance below [Fe/H] < -4.5 (Christlieb et al. 2004; Frebel et al. 2005, 2008; Norris et al. 2007; Caffau et al. 2011, 2016; Hansen et al. 2014; Keller et al. 2014; Allende Prieto et al. 2015; Bonifacio et al. 2015; Starkenburg et al. 2018; Aguado et al. 2018a,b).

The wide-field photometric survey *Pristine* has been especially designed to identify extremely metal-poor stars in an efficient manner (Starkenburg et al. 2017).[1] In contrast to many surveys that use stellar spectra to identify very metal-poor stars – i.e. *HK Survey*

★ E-mail: carmela.lardo@gmail.com

[1] *Pristine* reaches an ∼23 per cent success rate in detecting [Fe/H] ≤ -3 stars, whereas previous surveys have a success rate of $\leq$5 per cent (Aguado et al. 2019a).

Published by Oxford University Press on behalf of Royal Astronomical Society

(Beers, Preston & Shectman 1985, 1992), *Hamburg ESO Survey* (Christlieb et al. 2002, 2008; Frebel et al. 2005, 2006), *RAVE* (Steinmetz et al. 2006; Fulbright et al. 2010) – *Pristine* – like the *SkyMapper Southern Sky* (Keller et al. 2007; Wolf et al. 2018), the *S-PLUS* (Mendes de Oliveira et al. 2019; Whitten et al. 2021), and the *J-PLUS* (Cenarro et al. 2019) surveys – uses a photometric filter to isolate specific spectral regions that are sensitive to metallicity. Indeed, the *Pristine* Ca II H&K filter is centred on the lines of ionized calcium in the near ultraviolet that are extremely strong – and thus easily detectable – even at very low metallicities. Medium- and high-resolution spectroscopic follow-ups have been secured to fully characterize candidate metal-poor stars pre-selected by *Pristine* and study their chemical composition in great detail (Caffau et al. 2017, 2020; Youakim et al. 2017; Starkenburg et al. 2018; Bonifacio et al. 2019; Aguado et al. 2019a; Arentsen et al. 2020; Kielty et al. 2021; Venn et al. 2020).

Pristine_221.8781+09.7844 (Pr 221 hereafter) was first highlighted in the *Pristine* photometry as an extremely metal-poor star and it was followed up spectroscopically using the medium-resolution Intermediate-dispersion Spectrograph and Imaging System (ISIS) at the 4.2-m William Herschel Telescope (La Palma, Spain). This discovery led to the acquisition of high-resolution UVES spectra taken at the Kueyen 8.2-m Very Large Telescope (VLT; Paranal, Chile). The analysis of the high-resolution data confirmed the ultra-metal-poor nature of the star ([Fe/H] $= -4.66 \pm 0.13$) with an enhancement of 0.3–0.4 dex in α-elements and a remarkably low carbon abundance (Starkenburg et al. 2018). These authors were able to put an upper limit of $\log\epsilon(\mathrm{C}) \leq 5.6$ ([C/Fe] $\leq +1.76$), a value well below typical values in the ultra-metal-poor regime, suggesting that the star is carbon-normal (see the discussion in Starkenburg et al. 2018). This makes Pr 221 one of the three most metal-poor star (all metals included) known to date together with SDSS J102915+172927, a star with $[\mathrm{Fe/H}]_{\mathrm{LTE}} = -4.73$ ($[\mathrm{Fe/H}]_{\mathrm{NLTE}} = -4.60$) and carbon abundance $\log\epsilon(\mathrm{C}) \leq 4.3$ (Caffau et al. 2012) and HE 0557-4840 (Norris et al. 2007, 2012), a red giant branch (RGB) star with [Fe/H] $= -4.8$ and only a moderate enhancement in the C, N, and O abundances ([C/Fe] $= +1.1$, [N/Fe] $< +0.1$, and [O/Fe] $= +1.4$; all corrected for 3D effects; see Norris et al. 2012).

The ongoing low-resolution campaign to confirm the extremely and ultra-metal-poor candidates identified in *Pristine* photometry has yielded another interesting object: Pristine 237.8588+12.5660 (Pr 237 hereafter). Aguado et al. (2019a) measured a metallicity of [Fe/H] $= -3.88 \pm 0.08$ from the Ca II K line with a nearly flat *CH* band from the medium-resolution spectrum obtained with the Intermediate Dispersion Spectrograph (IDS) mounted on the 2.5-m Isaac Newton Telescope. From a high-resolution analysis, Kielty et al. (2021) determined a metallicity of [Fe I/H] ≤ -4.28 from the analysis of five Fe I lines. However, due to the limited wavelength coverage of their high-resolution spectra, the only elements whose abundances could be measured were lithium, magnesium, and calcium, whereas other key elements have only upper limits to their abundances.

At extremely low metallicities, stars typically show a somewhat high carbon abundance (e.g. Norris et al. 2013; Spite et al. 2013; Bonifacio et al. 2015; Hansen et al. 2016; Yoon et al. 2018; Rasmussen et al. 2020). Interestingly, this seems to be a function of the stellar metallicity, placing them all around the absolute C abundance of $\log\varepsilon\,(\mathrm{C}) \sim 6.3 \pm 0.5$. This, in turn, suggests that (i) first stars generally produced copious amounts of carbon during late stages of stellar evolution and/or their explosions (e.g. Umeda & Nomoto 2003; Meynet, Ekström & Maeder 2006; Ekström et al. 2008; Choplin et al. 2018) and (ii) a certain amount of metals available in the gas cloud out of which second-generation objects were formed might be needed to cool down, fragment, and eventually form low-mass stars (Frebel, Johnson & Bromm 2007). The existence of a class of ultra-metal-poor stars that are not severely carbon-enhanced therefore has enormous implications for the formation of low-mass stars at high redshifts.

In order to get further insight into the physics of early star formation and the properties of the first supernovae (SNe), it is important to fully characterize the abundance pattern and, in particular, the carbon content of these interesting objects. In this paper, we present and analyse new high-resolution observations of Pr 221 and Pr 237 to complement and expand the studies of Starkenburg et al. (2018), Aguado et al. (2019a), and Kielty et al. (2021).

This paper is organized as follows. In Section 2, we discuss the observations and data reduction. Section 3 contains a description of the stellar parameters and abundance derivations; Section 4 presents the abundance results. In particular, in Section 4.1, we focus on carbon abundances. In Section 4.4, we compare elemental abundances to a set of theoretical yields of zero-metallicity SNe to characterize the properties of the UMP progenitor SNe. Finally, we summarize our findings and draw the conclusions in Section 5.

2 OBSERVATIONS AND DATA REDUCTION

Observations were carried out with the UVES spectrograph (Dekker et al. 2000) between 2020 March 16 and 22 in delegated visitor mode, with relatively good atmospheric conditions, e.g. the typical seeing was around 1.0 arcsec. For these high-resolution observations, we used the standard setting DIC1 390+580 that covers the wavelength intervals 3300–4500 Å in the blue arm, and 4790–5760 and 5840–6800 Å in the red arm. The adopted set-up was combined with a slit width of 1 arcsec with 1 × 1 binning on the CCD. Observations were split in 14 and 15 observing blocks, respectively, for Pr 221 and Pr 237, corresponding to 14:45 and 13 h of total integration time.

UVES Spectra were reduced using the ESO Common Pipeline Library, UVES pipeline version 5.10.4.[2] The pipeline processing steps include bias subtraction, background subtraction optimal extraction, automatic sky subtraction, flat-fielding of the extracted spectra, wavelength calibration constructed from the Th-Ar lamp exposure, resampling at a constant wavelength step and optimal merging of the echelle orders.

The reduced spectra were then corrected for the barycentric velocity. Spectra shifted to the rest wavelength and smoothed to the resolution of 30 000 are combined as final step. Observations for Pr 221 were complemented with data from the DDT UVES programme (Programme 299.D-5042, which was using the same observational setup; see Starkenburg et al. 2018 for details). The approximate signal-to-noise ratio (S/N) per pixel of the final combined spectra are 90 at 4000 Å , 160 at 5300 Å, and 300 at 6700 Å. In Fig. 1, we show some selected spectral intervals of the analysed UVES spectra to illustrate the high-quality of the data.

2.1 Medium-resolution data

Pr 237 was also observed using the medium-resolution Optical System for Imaging and low-Intermediate-Resolution Integrated Spectroscopy (OSIRIS) spectrograph at the 10.4-m Gran Telescopio Canarias (GTC) located in the Roque de los Muchachos observatory (La Palma, Spain). We dedicated 1hr of GTC observing time to

---

[2] https://www.eso.org/sci/software/pipelines/uves/uves-pipe-recipes.html.

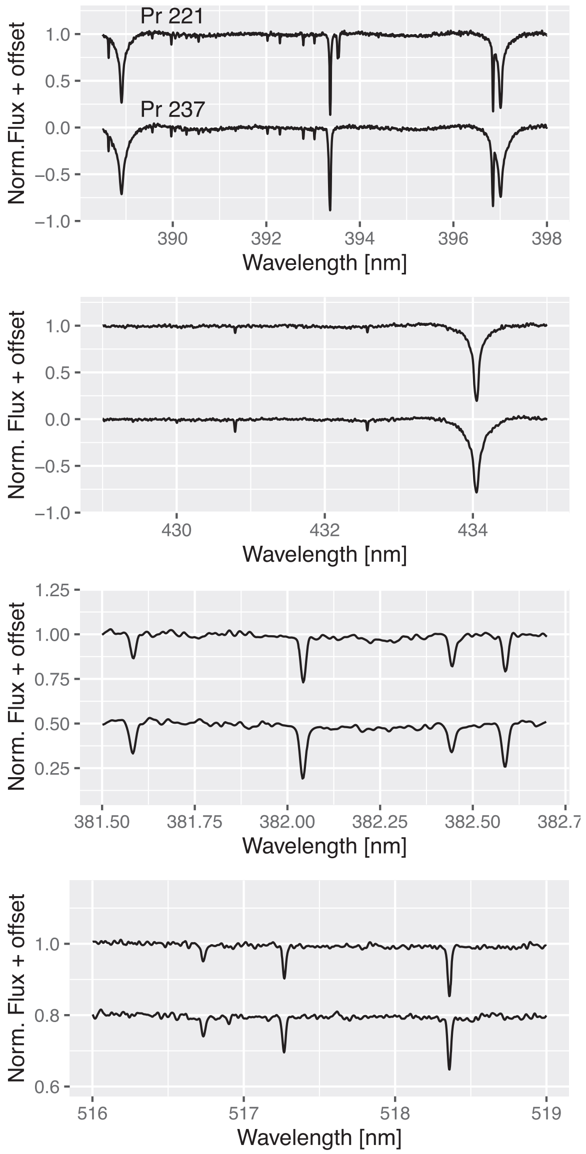

Figure 1. The figures shows (from the top to bottom) a detail of the UVES spectra of Pr 221 (upper spectrum) and Pr 237 (lower spectrum) around the Ca II H&K, the *CH* band, a zoom in the vicinity of the strong iron lines around 3820 Å, and the green Mg I *b* triplet.

obtain a long-slit spectrum with the R2500U VPH grating covering the spectral range 3440-4610 Å and 1.0-arcsec slit, leading to a resolving power of $R \sim 2400$. OSIRIS spectra were reduced in a standard manner including bias, flat-field correction, extraction, sky subtraction, and wavelength calibration. The mean S/N of the combined OSIRIS spectrum of Pr 237 is 170.

2.2 Radial velocity measurements

Radial velocities (RVs) have been derived using DAOSPEC (Stetson & Pancino 2008) on individual UVES exposures. The blue and red arms were analysed independently and the agreement between the two RV estimates is good (i.e. the difference is less than 1.5 km s^{-1} for both stars). The radial heliocentric velocity of the final spectrum is measured to be -149.25 ± 0.27 ($\sigma = 1.1$ km s^{-1}) and -3.18 ± 0.19 km s^{-1} ($\sigma = 0.7$ km s^{-1}) for Pr 221 and Pr 237, respectively. These derived values are in excellent agreement with those derived by Starkenburg et al. (2018) for Pr 221 (–149.0 ± 0.5 km s^{-1}) and Kielty et al. (2021) for Pr 237 (–3.8 ± 0.9 km s^{-1}).

Table 1. Position, photometry from SDSS DR13 (Albareti et al. 2017), and adopted stellar parameters for the two stars analysed in this study.

	Pr 221.8781+9.7844	Pr 237.8588+12.566
RA (J2000)	14:47:30.7	15:51:26.1
Dec. (J2000)	+09:47:03.70	+12:33:57.60
CaHK$_0$	16.87	15.84
g_0	16.51	15.58
i_0	16.04	15.30
RV (km s^{-1})	-149.25 ± 1.1	-3.18 ± 0.37
log (g) (dex)	3.03 ± 0.10	3.61 ± 0.10
$T_{\rm eff}$ (K)	5683 ± 134	6148 ± 175

For both stars, no significant velocity variations are measured on different exposures. Therefore, we have no evidence that these stars might be influenced by any binary companion and we continue with the assumption that the stars are single for the remainder of the paper. A complete discussion of the orbital properties in the Galaxy of the target stars can be found in Sestito et al. (2019, 2020) and Kielty et al. (2021).

RV measurements for the two stars analysed in this paper are listed in Table 1, along with other useful information.

3 CHEMICAL ANALYSIS

3.1 Stellar parameters

We derive stellar parameters following the approach outlined in Kielty et al. (2021). Briefly, effective temperature ($T_{\rm eff}$) is computed using the Mucciarelli & Bellazzini (2020) colour–$T_{\rm eff}$ relation, which combines effective temperatures derived by González Hernández & Bonifacio (2009) through the infrared flux method (IRFM) with the photometry available from the second release of the ESA/*Gaia* mission (Gaia Collaboration et al. 2016, 2018) and the *K*-band magnitudes from the 2MASS data base (Skrutskie et al. 2006). The adopted extinction coefficient from Schlafly & Finkbeiner (2011) are re-adapted for *Gaia* DR2 photometry.[3] Surface gravity (log g) was determined with the Stefan–Boltzmann equation and the bolometric correction for *Gaia* filters (Andrae et al. 2018). The stellar mass is treated as a flat prior, spanning a range from 0.5 to 1 M$_\odot$. Parallaxes are from *Gaia* DR2 (Gaia Collaboration et al. 2016, 2018).

The Mucciarelli & Bellazzini (2020) temperature calibration requires assumption about whether the star is a dwarf or giant and a value for the metallicity. In our computation, we assume a metallicity [Fe/H] = -4.0 ± 0.3 and use MIST/MESA isochrones (Paxton et al. 2011; Dotter 2016) to preliminary select between the dwarf/giant solution. Then we iterate the inference of the Mucciarelli & Bellazzini (2020) temperatures using the log g from Stefan–Boltzmann as input, and then again the log g with the new temperature. We did these iterations 1000 times to check for convergence or changes under small perturbations. Uncertainties associated with the atmospheric parameters are derived through Monte Carlo sampling of the input data taking into account the uncertainties associated with photometry, metallicity, distance, and extinction (e.g. Kielty et al. 2021).

---

[3] Gaia DR2 extinction relations are from http://stev.oapd.inaf.it/cgi-bin/cmd.

For Pr 221, we found $T_{\rm eff} = 5683 \pm 134$ K and $\log g = 3.03 \pm 0.10$. The derived stellar parameters are consistent with those derived in the studies of Sestito et al. (2019) ($T_{\rm eff}$ = 5710 ± 65 K, $\log g$ = 3.1 ± 0.1), and Starkenburg et al. (2018) ($T_{\rm eff}$ = 5792 ± 100 K, *e* $\log g$ = 3.5 ± 0.5), who adopted a slightly different approach to estimate atmospheric parameters. In Starkenburg et al. (2018), an effective temperature of $T_{\rm eff}^{\rm IRFM}$ = 5877 ± 62 K was derived using the IRFM of González Hernández & Bonifacio (2009) and a surface gravity of $\log g = 3.5$. Since the available photometry from 2MASS (Skrutskie et al. 2006) has too large uncertainties to be used to infer reliable temperatures, these derivations rely on the infrared UKIDSS *JHK* magnitudes (Lawrence et al. 2007) transformed into the 2MASS system and $V = 16.356 \pm 0.020$ from Henden et al. (2015). Magnitudes were dereddened $E(B - V) = 0.024$ from Schlegel, Finkbeiner & Davis (1998). The same method provides for each of the infrared UKIDSS *JHK* magnitudes (Lawrence et al. 2007) transformed into the 2MASS system very consistent values of $T_{\rm eff}^{\rm IRFM}$ = 5883 ± 77, 5878 ± 54, and 5871 ± 60 K for the *J*, *H*, and $K_{\rm s}$ band; respectively. Changing the surface gravity value from $\log g$ = 3.5 to 3.0 (as assumed here) would yield an effective temperature only 13 K hotter ($T_{\rm eff}^{\rm IRFM}$ = 5884 ± 62 K).

For Pr 237, we adopted $T_{\rm eff}$ = 6148 ± 175 K and $\log g$ = 3.61 ± 0.10 as in Kielty et al. (2021). The infrared 2MASS magnitudes $J = 14.509 \pm 0.035$, $H = 14.266 \pm 0.042$, and $K_{\rm s} = 14.257 \pm 0.060$ are also in this case not accurate enough to infer reliable temperatures. Unfortunately, no UKIDSS *JHK* infrared magnitudes are available for Pr 237. Using the 2MASS infrared magnitudes and assuming $V = 15.611 \pm 0.022$ (Henden et al. 2015) and reddening $E(B - V) = 0.039$ (Schlegel et al. 1998), we derive for Pr 237 $T_{\rm eff}^{\rm IRFM} = 6330 \pm 200$ K (González Hernández & Bonifacio 2009).

The effective temperatures derived from the Gaia photometry differ by Δ $T_{\rm eff} \sim -180$ K from those derived using ground-based photometry. With the available spectra, an inspection of the wings of the Balmer lines does not favour one solution over the other. The IRFM method requires accurate infrared photometry and reddening to estimate reliable temperatures. On the other hand, the Mucciarelli & Bellazzini (2020) calibration rely on all-sky, superb quality photometry from Gaia. Thus, we decided to use the Mucciarelli & Bellazzini (2020) calibration to estimate effective temperature and adopt the Kielty et al. (2021) procedure to derive stellar parameters. In Section 3.2, we discuss how the derived abundances would change because of the uncertainties on the atmospheric parameters.

3.2 Abundance measurements

3.2.1 High-resolution UVES data

We determined the chemical abundances for all the measured elements (except carbon and nitrogen) through the measurement of the equivalent widths (EWs) of atomic transition lines.

The atomic line list largely overlaps the one described in Starkenburg et al. (2018), except for the atomic data for the Mg I lines at 5172 and 5183 Å, for which we used the experimental log (*gf*)-values from Aldenius et al. (2007) and the predicted log (*gf*)-values from Yan & Drake (1995) for the Li I transition at 6707 Å. EWs were measured with the code DAOSPEC (Stetson & Pancino 2008) through the wrapper 4DAO (Mucciarelli 2013, 2017). Uncertainties on the EW measurements are estimated by DAOSPEC as the standard deviation of the local flux residuals and represent a 68 per cent confidence interval of the derived EW.

Elemental abundances from EWs were measured using the package GALA (Mucciarelli et al. 2013) based on the WIDTH9 code by Kurucz. Model atmospheres were calculated with the ATLAS9 code assuming local thermodynamic equilibrium (LTE) and one-dimensional, plane-parallel geometry; starting from the grid of models available on F. Castelli's website (Castelli & Kurucz 2003). The ATLAS9 models employed were computed with the new set of opacity distribution functions and exclude approximate overshooting in calculating the convective flux (Castelli & Kurucz 2003). We run GALA keeping $T_{\rm eff}$, log (g), and microturbulence of the model fixed, allowing its metallicity to vary in order to match the Fe abundance measured from EWs. For all the models, we adopted as input metallicity the iron abundances derived by Starkenburg et al. (2018) and Kielty et al. (2021). Only lines with a reduced EW (EWr = log (EW/λ)) between −5.9 (corresponding to ∼5.5 mÅ for a line at 4300 Å) and −4.7 (corresponding to ∼87 mÅ for a line at 4300 Å) were considered in the abundance analysis, in order to avoid weak and noisy lines as well as strong features in the flat part of the curve of growth. All the lines with EW uncertainties larger than 15 per cent[4] are also excluded. Finally, to compute the abundance of iron, we kept only lines within 3σ from the median iron value. In the analysis for this work the microturbulent velocity is fixed at 1.5 km s^{-1}. The solar values are all from Lodders, Palme & Gail (2009). For carbon and iron, we use the solar abundances of Caffau et al. (2011).

EW measurements for individual lines and corresponding elemental abundances are reported in Table 2. This table also lists the wavelength, excitation potential ($E_{\rm exc}$), and oscillator strengths (log (*gf*)) of the considered atomic transitions. The averaged results for each element are listed in Table 3. For the elements for which we measured more than one line, we provide in Table 3 the dispersion of the single line measurements around the mean normalized to the root square of the number of used lines that can be used to estimate the uncertainties associated with the measurements.

When the line-to-line scatter is relatively small (≤0.1 dex), the error is dominated by the errors due to the uncertainties in the stellar parameters. The error is dominated by the uncertainties associated with the derivation of atmospheric parameters, also in the case where only one line is measured for a given element. Uncertainties due to the atmospheric parameters are computed varying one parameter at a time by the corresponding error, while keeping the others fixed. They are listed in Table 4 for the two stars. All elements show a significant change with an ∼150-K variation in temperature. In contrast, changes in the adopted microturbulent velocity result in very small abundance variations for all elements. Finally, only abundances for those elements that appear in their ionized states (i.e. Ca II, Ti II, Sr II) are sensitive to changes in surface gravity.

The recommended error estimates associated with the measured abundances (e[X/H]) are summarized in Table 3.

3.2.2 Medium-resolution analysis of Pr 237

An estimate of the carbon content and metallicity of Pr 237 is obtained for the medium-resolution GTC/OSIRIS spectrum by comparing theoretical spectra with the observed one. Model atmospheres were computed with the KURUCZ codes as described in Mészáros et al. (2012). Modelled spectra were produced using synthesis code ASSϵT (Koesterke, Allende Prieto & Lambert 2008). We used the

---

[4] An error of ±15 per cent on EW measurements typically translates into an abundance error of ∼0.1 dex for a line located in the linear part of the curve of growth.

Table 2. EWs and associated LTE abundances for Pr 221 and Pr 237.

				Pristine_221.8781+09.7844				Pristine_237.8588+12.5660			
Ion	λ (Å)	log (gf)	$E_{\rm exc}$ (eV)	EW (mÅ)	σ EW (mÅ)	$\log\varepsilon$(X) LTE	NLTE	EW (mÅ)	σ EW (mÅ)	$\log\varepsilon$(X) LTE	NLTE
Li I	6707.77	0.17	0.00	9.40	0.45	1.33	1.31	10.60	0.55	1.74	1.72
Na I	5889.96	0.11	0.11	13.70	0.48	1.84	1.83				
Mg I	3829.36	− 0.23	2.71	24.00	0.85	3.14	3.48	20.00	1.38	3.34	3.63
	3832.30	0.13	2.71	50.20	1.87	3.29	3.65				
	5172.68	− 0.45	2.71	25.20	0.86	3.30	3.61	27.70	0.99	3.67	3.94
	5183.60	− 0.24	2.72	39.20	1.45	3.37	3.66	41.20	1.34	3.73	3.97
Al I	3961.52	− 0.33	0.01	8.90	0.26	1.38	2.06	6.80	0.79	1.65	2.25
Si I	3905.52	− 1.04	1.91	13.50	1.06	2.85	3.18				
Ca I	4226.73	0.24	0.00	35.00	1.58	1.77	2.07	28.20	1.61	2.05	2.31
Ca II	3933.66	0.11	0.11			2.22	2.17				
Sc II	4246.82	0.24	0.31	6.60	0.21	− 1.10					
Ti II	3759.29	0.28	0.61	28.80	0.44	0.39	0.53	46.30	0.72	1.17	1.29
	3761.32	0.18	0.57	33.50	1.51	0.55	0.69	46.40	0.63	1.24	1.35
	3913.46	− 0.36	1.12					7.10	0.34	1.15	1.21
	4300.04	− 0.46	1.18					8.10	0.40	1.34	1.49
	4395.03	− 0.54	1.08					7.60	0.54	1.29	1.40
Cr I	4254.34	− 0.11					0.00	5.70		<1.48	
Fe I	3758.23	− 0.03	0.96	32.30	0.56	2.53	2.92	36.10	1.44	3.09	3.36
	3763.79	− 0.24	0.99	25.50	1.08	2.61	3.00	29.80	1.23	3.19	3.47
	3767.19	− 0.39	1.01					21.10	0.50	3.14	3.42
	3787.88	− 0.86	1.01					18.20	1.36	3.53	3.80
	3815.84	0.23	1.48	23.20	0.23	2.58	3.05	30.70	0.77	3.20	3.55
	3820.43	0.12	0.86	48.50	0.63	2.62	3.02				
	3824.44	− 1.36	0.00	32.20	0.48	2.88	3.24	29.10	1.83	3.35	3.63
	3825.88	− 0.04	0.91	37.00	0.31	2.59	2.99	46.00	0.94	3.26	3.54
	3827.82	0.06	1.56	15.20	0.40	2.58	3.03	19.30	0.43	3.14	3.48
	3840.44	− 0.51	0.99	14.50	0.48	2.55	2.93	17.40	0.81	3.12	3.40
	3849.97	− 0.87	1.01	10.70	1.09	2.78	3.15	15.60	0.71	3.45	3.72
	3856.37	− 1.29	0.05	30.70	0.52	2.82	3.18	25.20	2.16	3.23	3.51
	3859.91	− 0.71	0.00	60.60	1.02	2.87	3.24	59.30	0.78	3.38	3.65
	3865.52	− 0.98	1.01	10.30	1.04	2.87	3.24	7.50	0.38	3.19	3.46
	3878.02	− 0.91	0.96	7.50	0.70	2.59	2.97	10.20	0.37	3.22	3.49
	3878.57	− 1.38	0.09	27.10	0.96	2.86	3.22	22.10	0.78	3.27	3.55
	3886.28	− 1.08	0.05	49.70	2.74	3.01	3.39				
	3895.66	− 1.67	0.11					8.40	0.92	3.08	3.35
	3899.71	− 1.53	0.09	19.10	0.61	2.80	3.16	17.00	0.52	3.28	3.55
	3902.95	− 0.47	1.56	8.30	0.44	2.80	3.21	14.00	0.43	3.49	3.80
	3920.26	− 1.75	0.12	12.90	0.56	2.84	3.20	12.60	0.47	3.36	3.63
	3922.91	− 1.65	0.05	17.10	0.31	2.82	3.18	13.90	0.42	3.25	3.53
	4005.24	− 0.61	1.56					10.20	0.54	3.46	3.74
	4045.81	0.28	1.48	28.30	0.47	2.63	3.06	40.30	0.55	3.33	3.64
	4063.59	0.06	1.56	16.70	0.23	2.61	3.01	27.90	1.17	3.34	3.64
	4071.74	− 0.02	1.61	14.40	0.21	2.66	3.06	21.20	0.44	3.30	3.60
	4143.87	− 0.51	1.56					10.10	0.58	3.35	3.63
	4202.03	− 0.71	1.48					8.20	0.73	3.37	3.66
	4260.47	0.08	2.40					8.10	0.46	3.43	3.72
	4271.76	− 0.16	1.48	14.60	0.75	2.67	3.09	22.60	0.77	3.35	3.66
	4325.76	0.01	1.61	14.10	0.33	2.60	3.03	23.00	0.77	3.30	3.62
	4383.54	0.20	1.48	29.10	0.21	2.69	3.13	35.30	0.17	3.27	3.59
	4404.75	− 0.14	1.56	19.10	0.91	2.85	3.26	22.30	0.59	3.38	3.68
	4415.12	− 0.62	1.61					9.50	0.34	3.45	3.74
	5269.54	− 1.32	0.86	11.10	0.51	2.97	3.35	10.00	0.55	3.42	3.70
Ni I	3858.30	− 0.87	0.42	5.50	0.61	1.54		5.50	0.31	2.04	
Sr II	4077.71	0.17	0.00	6.00	0.57	− 2.38	− 2.20	23.50	1.61	− 1.22	− 1.01
	4215.52	− 0.15	0.00					12.70	0.66	− 1.26	− 1.09
Y II	3774.33	0.21	0.13	5.90		< − 1.41					
Ba II	4934.07	0.15	0.00			< − 2.80				< − 2.10	
Eu II	4129.71	0.22	0.00	5.90		< − 1.59					

Notes. The corresponding NLTE abundances are also listed (see the text). Data for the atomic transitions analysed are also reported.

Table 3. Chemical abundances for Pr 221 and Pr 237.

		Pristine_221.8781+09.7844										Pristine_237.8588+12.5660									
		LTE				NLTE						LTE				NLTE					
Ion	$\log\varepsilon(X)_\odot$	$\log\varepsilon(X)$	[X/H]	[X/Fe]	σ	$\log\varepsilon(X)$	[X/H]	[X/Fe]	σ	e[X/H]	$N_{\rm lin}$	$\log\varepsilon(X)$	[X/H]	[X/Fe]	σ	$\log\varepsilon(X)$	[X/H]	[X/Fe]	σ	e[X/H]	$N_{\rm lin}$
Li I	1.10	1.33	0.23	5.02		1.31	0.21	4.61		0.20	1	1.74	0.64	4.86		1.72	0.62	4.55		0.20	1
CH	8.50	<6.00	<−2.50	<2.29							1	<6.30	<−2.20	<2.02							1
NH	7.86	<5.00	<−2.86	<1.93							1	<6.00	<−1.86	<2.36							1
Na I	6.30	1.84	−4.46	0.33		1.83	−4.47	−0.07		0.10	1										
Mg I	7.54	3.28	−4.26	0.53	0.10	3.60	−3.94	0.46	0.08	0.10	4	3.58	−3.96	0.26	0.21	3.85	−3.69	0.24	0.19	0.13	3
Al I	6.47	1.38	−5.09	−0.30		2.06	−4.41	−0.01		0.11	1	1.64	−4.83	−0.61		2.24	−4.23	−0.30		0.15	1
Si I	7.52	2.85	−4.67	0.12		3.18	−4.34	0.06		0.11	1										
Ca I	6.33	1.77	−4.56	0.23		2.07	−4.26	0.14		0.13	1	2.05	−4.28	−0.06		2.31	−4.02	−0.09		0.16	1
Ca II	6.33	2.22	−4.11	0.68		2.17	−4.16	0.24		0.14	1										
Sc II	3.10	−1.10	−4.20	0.59						0.08	1										
Cr I	5.64											1.48	<−4.16	<0.06							1
Ti II	4.90	0.47	−4.43	0.36	0.12	0.61	−4.29	0.11	0.11	0.09	2	1.24	−3.66	0.56	0.08	1.35	−3.55	0.38	0.11	0.13	5
Fe I	7.52	2.73	−4.79		0.14	3.12	−4.40		0.13	0.14	27	3.30	−4.22		0.12	3.59	−3.93		0.12	0.17	33
Ni I	6.23	1.54	−4.69	0.10						0.15	1	2.04	−4.19	0.03						0.19	1
Sr II	2.92	−2.38	−5.30	−0.51		−2.2	−5.12	−0.72		0.09	1	−1.24	−4.16	0.06	0.03	−1.05	−3.97	−0.04	0.06	0.12	2
Ba II	2.17	<−2.80	<−4.97	<−0.18							1	<−2.1	<−4.27	<−0.05							1

FERRE[5] code (Allende Prieto et al. 2006) to search for the best fit to the observed spectrum by simultaneously deriving the metallicity [Fe/H] and the carbon abundance [C/Fe] while keeping atmospheric parameters fixed to the values derived in Section 3.1.

3.3 NLTE calculations

At very low metallicities, non-local thermodynamic equilibrium (NLTE) effects are often significant (Asplund 2005). The electron density decreases and the collision rates are greatly reduced with decreasing metal abundance. Furthermore, the radiation is absorbed by a smaller fraction of metal atoms and ions and the photoionization rate increases (Gehren et al. 2004). Since the departures of the excitation and ionization states of the elements from the thermodynamic equilibria are more extreme in metal-poor and hotter atmospheres, the NLTE abundances provide a more realistic picture of the overall chemical pattern of our unevolved UMP targets.

As a first attempt to determine the NLTE abundance patterns that can be compared with Population III SN nucleosynthesis yields, we performed the NLTE calculations for Na I, Mg I, Al I, Si I, Ca I–II, Ti I–II, Fe I–II, and Sr II, using the NLTE methods developed in our earlier studies and based on the most up-to-date atomic data available so far. In metal-poor atmospheres, collisional rates are mainly determined by collisions with neutral hydrogen atoms. For Na I (Alexeeva, Pakhomov & Mashonkina 2014), Mg I (Mashonkina 2013), Al I (Baumueller & Gehren 1996; Mashonkina, Belyaev & Shi 2016), Si I (Mashonkina 2020), Ca I-II (Mashonkina, Korn & Przybilla 2007; Mashonkina, Sitnova & Belyaev 2017a), and Sr II (Belyakova & Mashonkina 1997; Mashonkina 2021), collisions with H I atoms were treated by implementing the quantum-mechanical rate coefficients from calculations of Barklem et al. (2010, Na I), Barklem et al. (2012, Mg I), Belyaev (2013, Al I), Belyaev, Yakovleva & Barklem (2014, Si I), Belyaev et al. (2017, Ca I), and Mashonkina (2021, Sr II). For Ti I–II and Fe I–II, we used the Drawinian rates (Steenbock & Holweger 1984) scaled by $S_{\rm H} = 1$ and 0.5, respectively, according to empirical estimates of Sitnova, Mashonkina & Ryabchikova (2016) and Mashonkina et al. (2011). The coupled radiative transfer and statistical equilibrium equations were solved with the code DETAIL (Butler & Giddings 1985), where the opacity package was revised as presented by Mashonkina et al. (2011).

Table 4. Changes of the derived elemental abundances depending on stellar parameters.

Ion	$+\Delta\ T_{\rm eff}$	$-\Delta\ T_{\rm eff}$	$+\Delta\log g$	$-\Delta\log g$	$+\Delta\ v_{\rm t}$	$-\Delta\ v_{\rm t}$
Pristine_221.8781+09.7844						
$\Delta T_{\rm eff} = 134$ K, $\Delta\log g = 0.1$ dex, $\Delta v_{\rm t} = 0.5$ km s^{-1}						
Fe I	0.13	−0.13	−0.00	0.00	−0.03	0.04
Li I	0.10	−0.10	−0.00	0.00	0.01	−0.03
Na I	0.09	−0.10	−0.00	0.00	−0.01	0.01
Mg I	0.08	−0.09	−0.00	0.00	−0.02	0.03
Al I	0.10	−0.11	−0.00	0.00	−0.01	0.01
Si I	0.10	−0.11	0.00	−0.00	−0.01	0.01
Ca I	0.11	−0.12	−0.00	0.00	−0.04	0.05
Ca II	0.13	−0.14	−0.02	0.01	−0.02	0.01
Sc II	0.07	−0.08	0.03	−0.03	−0.01	0.01
Ti II	0.07	−0.07	0.03	−0.03	−0.04	0.05
Ni I	0.13	−0.14	−0.00	0.00	−0.01	0.01
Sr II	0.08	−0.08	0.03	−0.03	−0.01	0.01
Pristine 237.8588+12.5660						
$\Delta T_{\rm eff} = 175$ K, $\Delta\log g = 0.1$ dex, $\Delta v_{\rm t} = 0.5$ km s^{-1}						
Fe I	0.17	−0.17	−0.00	0.00	−0.03	0.05
Li I	0.13	−0.13	−0.00	0.00	0.01	−0.03
Mg I	0.11	−0.12	−0.00	0.00	−0.03	0.03
Al I	0.14	−0.14	0.00	0.00	−0.00	0.00
Ca I	0.15	−0.16	−0.00	0.00	−0.03	0.03
Ti II	0.09	−0.09	0.03	−0.03	−0.06	0.09
Cr I	0.17	−0.18	−0.00	0.00	−0.01	0.01
Ni I	0.18	−0.19	−0.00	0.00	−0.01	0.01
Sr II	0.11	−0.11	0.03	−0.03	−0.02	0.03

For Li I, we applied the NLTE abundance corrections from Lind, Asplund & Barklem (2009). In the literature, there are no NLTE corrections for lines of Sc II, Cr I, and Ni I for atmospheric parameters relevant to the analysed stars. Thus, we provide only LTE abundances for those elements.

Line-to-line elemental abundances corrected for NLTE are in Table 2. The NLTE effects turn out to be rather small ($\Delta_{\rm NLTE} = \log\varepsilon_{\rm (NLTE)} - \log\varepsilon_{\rm (LTE)} \leq 0.05$ dex) for Li I, Na I, and Ca II. On the

---

[5] Available from http://github.com/callendeprieto/ferre.

other hand, significant abundance shifts were found for the minority species that are subject to overionization, such as Mg I, Al I, Ca I, and Fe I, with positive $\Delta_{\rm NLTE}$ corrections always larger than 0.3 dex.

3.4 Comments on individual elements

Lithium was detected in both stars, although we note that the continuum determination may have a significant impact on the measured abundances (see also Starkenburg et al. 2018).

We measured the 5890 Å line of Na I for Pr 221, being the same line in Pr 237 distorted by interstellar absorption. The blue Mg triplet and green Mg I b lines were detected in both spectra and their resulting abundances are in good agreement. Al was measured from the Al I 3961 Å line, since the other Al I line at 3944 Å line is severely contaminated by CH features. It was possible to detect usable Si I and Sc II lines only in the Pr 221 spectrum.

For both objects, Ca abundances were derived from the Ca I line at 4226 Å. For Pr 221, we also measured the calcium abundance from the synthesis of the Ca II K line. The abundances in LTE differ by 0.45 dex, with a higher Ca II abundance. However, the observed discrepancy is greatly reduced when abundances are corrected for NLTE. In Section 3.6 we use ionization equilibrium of calcium as a consistency check on the surface gravity value adopted for Pr 221 from photometry.

Abundances for Ti II were measured from two and five lines for Pr 221 and Pr 237, respectively. A Cr I feature at 4254 Å can be detected in the spectrum of Pr 237, however such line is extremely weak and therefore extremely noisy and sensitive to the continuum placement. Thus, the provided value should be regarded as an upper limit to the actual Cr I abundance measurement. Abundances for Ni I have been derived from the blue feature at 3858 Å. Sr II measurements are based on just one line in Pr 221 and two lines in Pr 237.

In Table 3, we also provide upper limits for Y II, and Eu II. For these elements, there is considerable uncertainty in the measurement of the EWs because they are weak (i.e. <10 mÅ) and noisy.

3.5 Carbon and nitrogen

We use spectrum synthesis to analyse features of CH and NH and constrain the abundances of carbon and nitrogen. The synthetic spectra were computed with the SYNTHE code developed by Kurucz (Kurucz 2005) in its Linux version (Sbordone 2005) and adopting the same model atmospheres used to derive the abundances from EWs. The molecular line list are taken from Masseron et al. (2014) and the latest Kurucz compilation.[6]

The C abundance is determined from the CH lines in the *G* band (the region between 4309–4314 and 4365–4369 Å) that are almost free from atomic blends. For Pr 221, further constraints on carbon abundances are obtained from the CH 3944 Å line, which blends the Al I resonance line at 3944 Å. Such line was shown by Arpigny & Magain (1983) to be severely blended with several CH lines, even in stars where CH was not a prominent feature of the spectrum. Corrections for the effect of evolutionary status on carbon are negligible (i.e. less than 0.01) for both stars, because of their unevolved nature (Placco et al. 2014).

An upper limit to the nitrogen abundance is derived for both stars from the ultraviolet NH band $A^3\Pi_i - X^3\Sigma^-$ at 3360 Å.

3.6 Consistency check on atmospheric parameters

Calcium is observed in two ionization stages in the spectrum of Pr 221. From the Ca I line at 4226 Å, we measure an abundance of $\log\varepsilon$ (Ca) = 1.77 ± 0.12, whereas the analysis of the Ca II line at 3933 Å gives $\log\varepsilon$ (Ca) = 2.22 ± 0.14. Both lines are subject to departures from LTE, however, the NLTE corrections for the two lines are different. For the Ca I line at 4226 Å, NLTE raises the abundance by 0.3 dex and leads to an NLTE abundance of $\log\varepsilon$ (Ca) = 2.07. Conversely, the NLTE correction for Ca II line at 3993 Å is slightly negative (–0.04 dex). This brings the abundances derived from lines of the two ionization stages in good agreement. Thus, we conclude that the Ca I/Ca II ionization equilibrium is fulfilled for the atmospheric parameters we have adopted for Pr 221.

4 RESULTS

4.1 Constraints on the C and N abundances

Starkenburg et al. (2018) were able to put an upper limit of $\log\varepsilon({\rm C}) \leq 5.6$ to the carbon abundance of Pr 221 using the WHT/ISIS spectrum at intermediate resolution (R ∼ 2400). Despite the relatively good S/N of their high-resolution UVES spectrum (S/N ∼ 45 at 4000 Å), the quality of the data was not sufficient to detect carbon enhancement below the level already set by the higher S/N medium-resolution spectrum.

Because of the low metallicity and the relatively high effective temperatures of the target stars, large changes in carbon abundances have an extremely small impact on the appearance of the (weak) CH absorption. The synthetic spectra of Fig. 2 show that the difference between $\log\varepsilon({\rm C}) = 5.5$ and 6 never exceeds the 2 per cent of the flux. Despite the noise and the uncertainties in the continuum placement, it seems that the theoretical spectrum with $\log\varepsilon({\rm C}) \leq 6.0$ ([C/Fe] ≤ +2.29) presents a conservative upper limit to the carbon abundance. However, the S/N of the combined UVES spectrum of Pr 221 is still too low to permit accurate analysis of individual CH lines at the wavelengths shown in Fig. 2.

As noted by Arpigny & Magain (1983), the Al I line at 3944 Å is severely contaminated by CH. We used the 3944-Å blend to check the estimated C abundance of Pr 221. The aluminium NLTE and LTE abundances were fixed from analysis of the second line of the resonance doublet, Al I 3961 Å. Since the NLTE abundance corrections for Al I 3944 and 3961 Å are equal, in this section, we perform analysis of these lines under the LTE assumption. Fig. 3 (top left-hand panel) shows that $\log\varepsilon({\rm Al\,I}) = 1.38$ represents the best LTE fit to the observed spectrum of Al I 3961 Å.

The same Fig. 3 also shows the impact of different carbon abundances on the synthetic spectra computed around the Al I line at 3944 Å. An increasing abundance of carbon mainly enhances the spectral feature at the blue end of the Al I 3944 Å line. If one assumes that the blue wing is noise and that $\log\varepsilon({\rm C}) = 5.0$ (top right-hand panel of Fig. 3), we derive an abundance of $\log\varepsilon({\rm Al\,I}) = 1.54$, which is greater than the value measured from the fit of the Al I line at 3961 Å. This indicates, that the solution with $\log\varepsilon$ (C) = 5.0 is not favoured, since carbon should be more abundant to contribute to the left wing of the Al I 3944 Å blend.

The model with $\log\epsilon$ (C) = 5.5 and $\log\varepsilon({\rm Al\,I}) = 1.38$ seems to reproduce well the observed Al I 3944 Å feature, and in this case, the derived Al abundance agrees with that inferred from the clean Al I 3961 Å. The $\log\varepsilon$ (C) = 5.5 value is lower than the C abundance deduced from the *G* band and supports our conclusion that Pr 221 does not belong to strongly C-enhanced stars.

---

[6] http://wwwuser.oat.ts.astro.it/castelli/linelists.html.

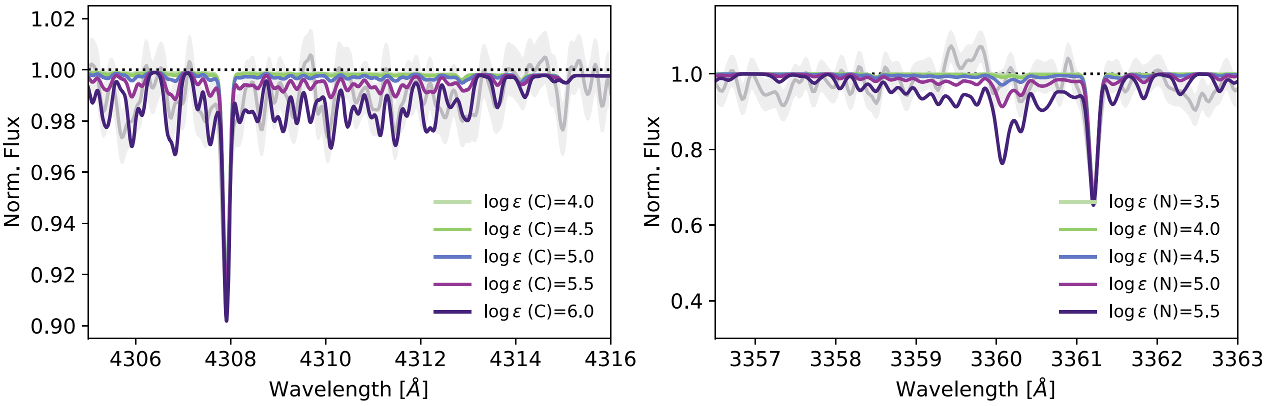

Figure 2. The comparison of the UVES high-resolution spectrum of Pr 221 (thick grey line) with model spectra with with $T_{\rm eff} = 5683$ K, $\log{(g)} = 3.03$, [M/H] $= -4.79$, and varying carbon and nitrogen abundances (see the legend) is shown in the left- and right-hand panels, respectively. The noise level is represented by the grey shaded area. All synthetic spectra are smoothed to a resolution of $R = 30\,000$.

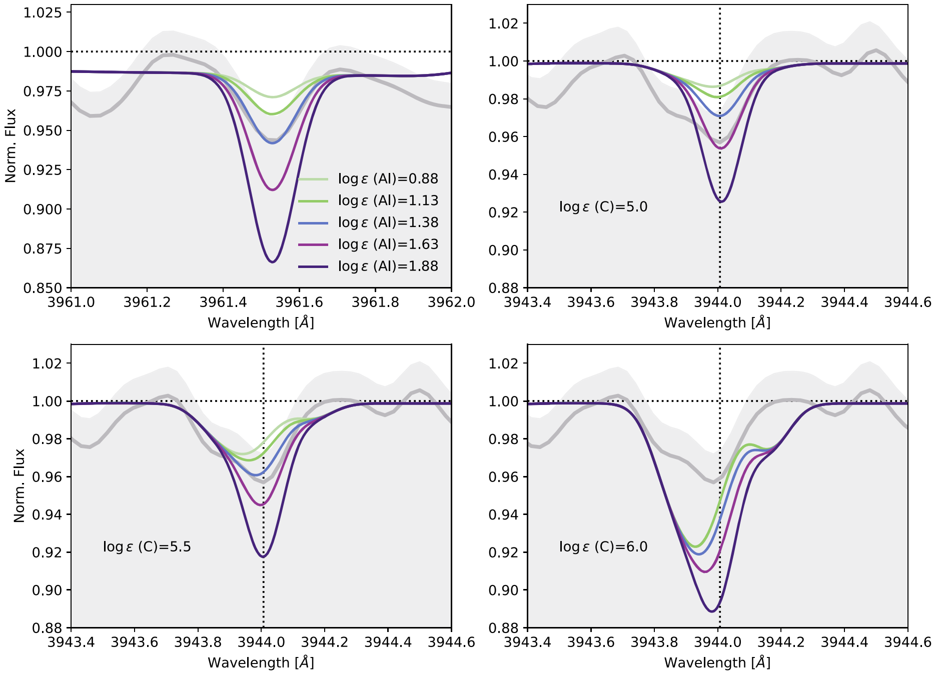

Figure 3. The top left-hand panel shows synthetic spectra with (from the top to bottom) $\log \varepsilon$(Al) $= 0.88$, 1.13, 1.38, 1.63, and 1.88 around the Al I line at 3961 Å. The effects of changing aluminium abundances by the same amounts for the modelled spectra around the Al I 3944 Å line are plotted for different carbon abundances $\log \epsilon$ (C) $= 5.0$, 5.5, and 6.0 (top right-hand, bottom left-hand, and bottom right-hand panels, respectively). All modelled spectra are smoothed to a resolution of $R = 30\,000$. The observed spectrum of Pr 221 is shown as a grey thick line in all panels. The noise level is represented by the grey shaded area.

Fig. 2 shows the observed spectrum of Pr 221 around the *NH* band at 3360 Å. From the comparison of the observed spectrum with synthetic ones with varying nitrogen abundances, we estimate an upper limit of $\log \varepsilon$ (N) ≤ 5.0 to the nitrogen content of Pr 221.

In Fig. 4, we compare the UVES spectrum of Pr 237 with theoretical models with varying carbon and nitrogen abundances. Because of the high effective temperature and low metallicity, models spanning a large range in carbon abundances (from $\log \epsilon$(C) $= 5.0$ to 6.5) differ by less than 2 per cent of the flux. Thus, despite the high quality of the data, we are only able to put an upper limit to the C abundance of $\log \varepsilon$ (C) < 6.3. This would correspond to to [C/Fe] $< +2.02$, when taken together with the high-resolution measurement of iron, [Fe/H] $= -4.22$. A similar upper limit of [C/Fe] < 1.90 can be derived by the medium-resolution spectrum using metallicity from the high-resolution UVES spectrum. When the measured carbon abundance is taken together with the metallicity derived from FERRE from the medium-resolution data, the upper limit to the carbon abundance is [C/Fe] $< +2.10$ (see also Fig. 5).Therefore, we assume $\log \varepsilon$ (C) < 6.3 as a conservative upper limit to the carbon abundance of Pr 237. From a careful inspection of the right-hand panel of Fig. 4, we adopt $\log \varepsilon$ (N) ≤ 6.0 as the upper limit for the nitrogen abundance of Pr 237.

Due to the reduced radiative heating with a shortage of spectral lines, the temperature structures of metal-poor 3D hydrodynamical model atmospheres are much cooler in the higher atmospheric layers (e.g. Asplund 2005). This translate into large 3D effects for

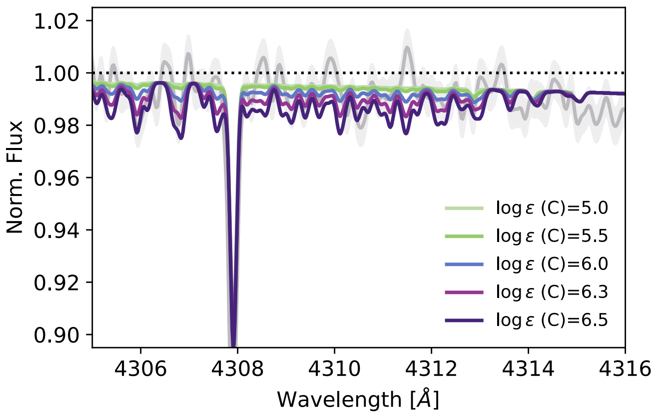

Figure 4. The same as for Fig. 2 for Pr 237.

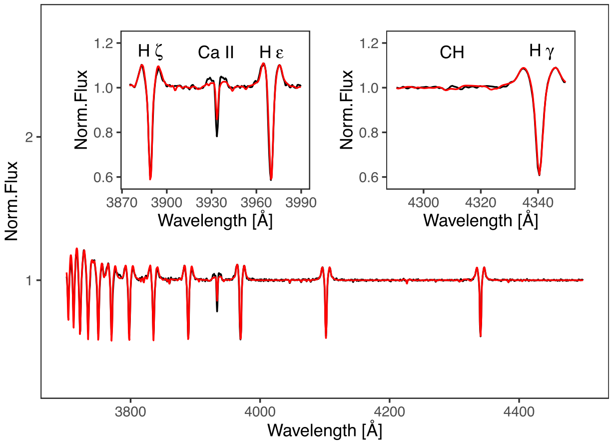

Figure 5. The medium-resolution spectrum for Pr 237 as observed with GTC/OSIRIS and normalized by a running mean by the FERRE code is shown in black. The best-fitting spectrum –with the same normalization – is overplotted in red. The insets display a zoom around the Ca II K line and the *G* band.

temperature-sensitive species like molecules (see e.g. Asplund & García Pérez 2001; Collet, Asplund & Trampedach 2007; González Hernández et al. 2010; Gallagher et al. 2016, 2017; Nordlander et al. 2017; Collet et al. 2018). The complete 3D analysis of target stars is beyond the scope of this study, but we refer to the 3D corrections derived by Caffau et al. (2012) for SDSS J102915+172927 – a star with stellar parameters and abundances similar to Pr 221 (see discussion in Starkenburg et al. 2018) – to give a qualitative idea of the corrections expected for the carbon and nitrogen abundances discussed here. The work of Caffau et al. (2012) shows that the use of 3D, LTE modelling (as opposed to our 1D, LTE procedure) would lead to significantly lower abundances for both carbon and nitrogen (by −0.7 and −0.9 dex, respectively). Unfortunately, no detailed calculations for departures from LTE for CH and NH with realistic molecular models exist.

4.2 Overall chemical pattern

We measured the EWs of 27 Fe I lines for the combined spectrum of Pr 221, which yield a final LTE abundance of $[\mathrm{Fe\,I/H}]_{\mathrm{LTE}} = -4.79 \pm 0.14$. This corresponds to $[\mathrm{Fe\,I/H}]_{\mathrm{NLTE}} = -4.40 \pm 0.13$. From the analysis of 33 Fe I lines in the UVES spectrum of Pr 237, we measure $[\mathrm{Fe\,I/H}]_{\mathrm{LTE}} = -4.22 \pm 0.12$ and $[\mathrm{Fe\,I/H}]_{\mathrm{NLTE}} = -3.93 \pm 0.12$. The medium-resolution analysis of the GTC/OSIRIS spectrum returns a higher metallicity of $[\mathrm{Fe/H}] = -3.86 \pm 0.20$ dex.

Fig. 5 shows the observed GTC/OSIRIS spectrum normalized by a running mean by FERRE along with the best-fitting model –with the same normalization (Aguado et al. 2017a,b). The metallicity $[\mathrm{Fe/H}] = -3.86$ dex derived from the GTC/OSIRIS spectrum is in good agreement with what is found from the high-resolution UVES analysis under the NLTE assumption ($[\mathrm{Fe/H}]_{\mathrm{NLTE}} = -3.93 \pm 0.12$). This is because – due to the extreme weakness of most of the absorption lines – most information for the metallicity determination in the intermediate-resolution data comes from the Ca II K line, for which NLTE corrections are extremely small (∼−0.02 dex). However, we also note that the Ca II K is blended with with an interstellar Ca absorption line in the GTC/OSIRIS spectrum. This may also account for the higher metallicity derived from intermediate-resolution spectrum relative to the UVES one.

In the low-metallicity regime, and increasing fraction of MW halo stars has been found to be greatly enhanced in carbon, the so-called carbon-enhanced metal-poor (CEMP) stars (e.g. Beers & Christlieb 2005). Depending on their abundance pattern, CEMP stars have been traditionally classified in several subclasses: CEMP-s, CEMP-r, CEMP-r/s, and CEMP-no (Beers & Christlieb 2005).[7] The high carbon enhancement accompanied by strong overabundances of neutron-capture elements produced by the main *s*-process observed in both CEMP-s and CEMP-r/s stars is thought to be produced by mass-transfer from low- to intermediate-mass (from 1 to 4 $\mathrm{M}_{\odot}$) asymptotic giant branch (AGB) companion (e.g. Starkenburg et al. 2014; Abate et al. 2015; Hansen et al. 2015; Sakari et al. 2018; Choplin, Siess & Goriely 2021).

In contrast, the carbon enhancement with low (or absent) abundances of neutron-capture elements observed in CEMP-no stars is thought to reflect directly the composition of the natal gas cloud from which the star first formed. Several astrophysical sites have been proposed for the progenitors of these bona-fide second-generation stars, including 'faint SNe' that undergo mixing and fallback (e.g. Tominaga, Iwamoto & Nomoto 2014; Komiya et al. 2020), rapidly rotating massive stars of ultra-low-metallicity (e.g. Meynet et al. 2006; Chiappini et al. 2008; Maeder, Meynet & Chiappini 2015; Choplin et al. 2016), and metal-free massive stars (Heger & Woosley 2010).

---

[7] CEMP-s : $[\mathrm{C/Fe}] > +1.0$, $[\mathrm{Ba/Fe}] > +1.0$, and $[\mathrm{Ba/Eu}] > +0.5$; CEMP-r: $[\mathrm{C/Fe}] > +1.0$ and $[\mathrm{Eu/Fe}] > +1.0$; CEMP-r/s: $[\mathrm{C/Fe}] > +1.0$ and $0.0 < [\mathrm{Ba/Eu}] < +0.5$ CEMP-no: $[\mathrm{C/Fe}] > +1.0$ and $[\mathrm{Ba/Fe}] < 0.0$.

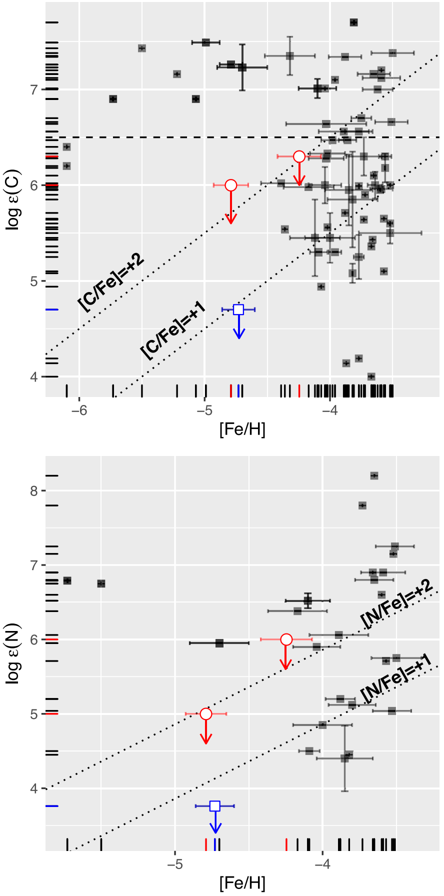

Figure 6. C and N abundances for the two stars compared to literature values. Red empty circles are the two targets analysed in this study, whereas the blue empty square represents SDSS J102915+172927 (Caffau et al. 2011), the most metal-poor star observed so far with a similar overall chemical pattern to Pr 221 (see Starkenburg et al. 2018, for a discussion). Stars from literature with [Fe/H] ≤ -3.5 and log $(g) \ge 3$ are shown as black symbols. The horizontal dashed line in the top panel gives the mean log ε (C) = 6.5 value used by Spite et al. (2013) to define carbon enhanced metal-poor stars at metallicities [Fe/H] < -3.4.

In Fig. 6, [C/Fe] and [N/Fe] LTE abundances are shown as a function of [Fe/H] for Pr 221 and Pr 237 and unevolved stars (e.g. log $g \ge 3$) with metallicities lower than [Fe/H] < -3 collected from the SAGA data base.[8] In the figure, Pr 221 and Pr 237 are represented as empty red circles, whereas data from the literature are shown as black filled squares. In the same figure we also highlight SDSS J102915+172927 (shown as empty blue square; Caffau et al. 2011), the star with lowest metallicity known. Inspection of the top panel of Fig. 6 leads us to conclude that both Pr 221 and Pr 237 belong to the group of low-carbon band (Bonifacio et al. 2015) with both stars possibly being 'carbon-normal'.[9] Both stars are classified as CEMP-no stars, as they do not show any overabundance of neutron-capture elements (see Section 4.2) and they are associated with the low-C region (log ε (C) $\le$ 7.1; Yoon et al. 2016). Additionally, among the CEMP-no sample itself, two very different behaviours in the log ε(C) versus [Fe/H] space can be observed and they are likely associated with different classes of progenitors (Yoon et al. 2016). In particular, both stars would be classified as Group II CEMP-no stars (e.g. stars for which a clear dependence of log ε (C) on [Fe/H] is observed; see the top panel of Fig. 6)[10] and they can be tentatively associated faint mixing-and-fallback SNe progenitors (Nomoto, Kobayashi & Tominaga 2013).

Similarly to carbon, also nitrogen appears to be underabundant in Pr 221 when compared to stars of similar metallicity. However, only a few measurements of N abundance exist at this low-metallicity regime to draw firm conclusions.

In Fig. 7, the absolute abundance of Li (log ε (Li)), as well as abundance ratios [X/Fe] for 11 representative elements (X) in LTE are shown as a function of [Fe/H], for Pr 221, Pr 237, and stars with metallicities lower than [Fe/H] < -3 taken from the SAGA data base.[11] In this figure, Pr 221 and Pr 237 are represented as empty red circles, whereas data from literature are shown as black filled squares.

The measured lithium abundances is log ε (Li I)$_{\rm LTE}$ = 1.33 and 1.74 for Pr 221 and Pr 237, respectively. The uncertainties we derive from the EW measurements are extremely small for both objects (0.02 dex), but a more realistic determination of the uncertainties associated with Li I measurements of 0.2 dex can be obtained taking into account uncertainties due to the continuum placement (e.g. Starkenburg et al. 2018; Kielty et al. 2021). Fig. 8 shows synthetic spectra around the Li I resonance line for Pr 221 and Pr 237. The best-fitting solution is shown along with synthetic spectra with Li I abundance changed by Δ log ε (Li I) = ± 0.2 and 0.4. The top left-hand panel of Fig. 7 we compare the absolute Li abundances derived for the two stars with log ε (Li) values form the literature for stars with surface gravities log $g > 3$. Both stars have Li I abundance below the plateau found by Spite & Spite (1982a), Spite & Spite (1982b) for old and unevolved stars. This is in line with observations of stars with [Fe/H] ≤ -3 (Sbordone et al. 2010), with the notable exception of the dwarf star J0023+0307 with an [Fe/H] < -6.1 and a Li abundance of log ε(Li I) = 2.02 ± 0.08 dex (Aguado et al. 2019b). For Pr 221, the observed Li I abundance can also be ascribed to its relatively low effective temperature. We refer to González Hernández et al. (2019, 2020) for a complete discussion on Li abundances in EMP/UMP stars.

The [Na/Fe] and [Al/Fe] LTE ratios appear to vary from star to star by a very large factor at lower metallicities (see Fig. 7). The scatter of data for stars of close metallicity is, in part, due to neglecting the departures from LTE. For [Fe/H] <-3, the Na and Al abundances can only be derived from resonance lines, for which the NLTE effects are strongly dependent on atmospheric parameters and element abundance itself (Baumueller & Gehren 1997; Baumueller, Butler & Gehren 1998). For Pr 221, the NLTE abundance of Na is found to be lower than the LTE abundance, by 0.40 dex, while, in contrast, the Al abundance is higher in NLTE than in LTE, by 0.68 dex. NLTE correction of +0.60 dex was calculated for Al I 3961 Å in Pr 237. With the NLTE effects taken into account, we retrieve [Na/Fe] and [Al/Fe] abundance ratios close to their solar values, in line with available NLTE studies of the EMP stars (Andrievsky et al. 2007; Bonifacio et al. 2009; Mashonkina et al. 2017b) and the predictions by Samland (1998) for the Galactic [Na/Fe] versus [Fe/H] trend.

---

[8] Available at http://sagadata base.jp.

[9] Bonifacio et al. (2015) define 'carbon-rormal' stars with [Fe/H] < -4 and log ε(C)$\le$ 5.5 or [Fe/H]≥ -4 and [C/Fe] $< +1.0$. Low-carbon band are stars that do not fulfil the 'carbon normal' criterion and have log ε(C) $\le$ 7.6.

[10] This conclusion is further supported by the measured abundance of the light-elements Na and Mg in the two stars (see fig. 4 in Yoon et al. 2016).

[11] Aivalable at http://sagadata base.jp.

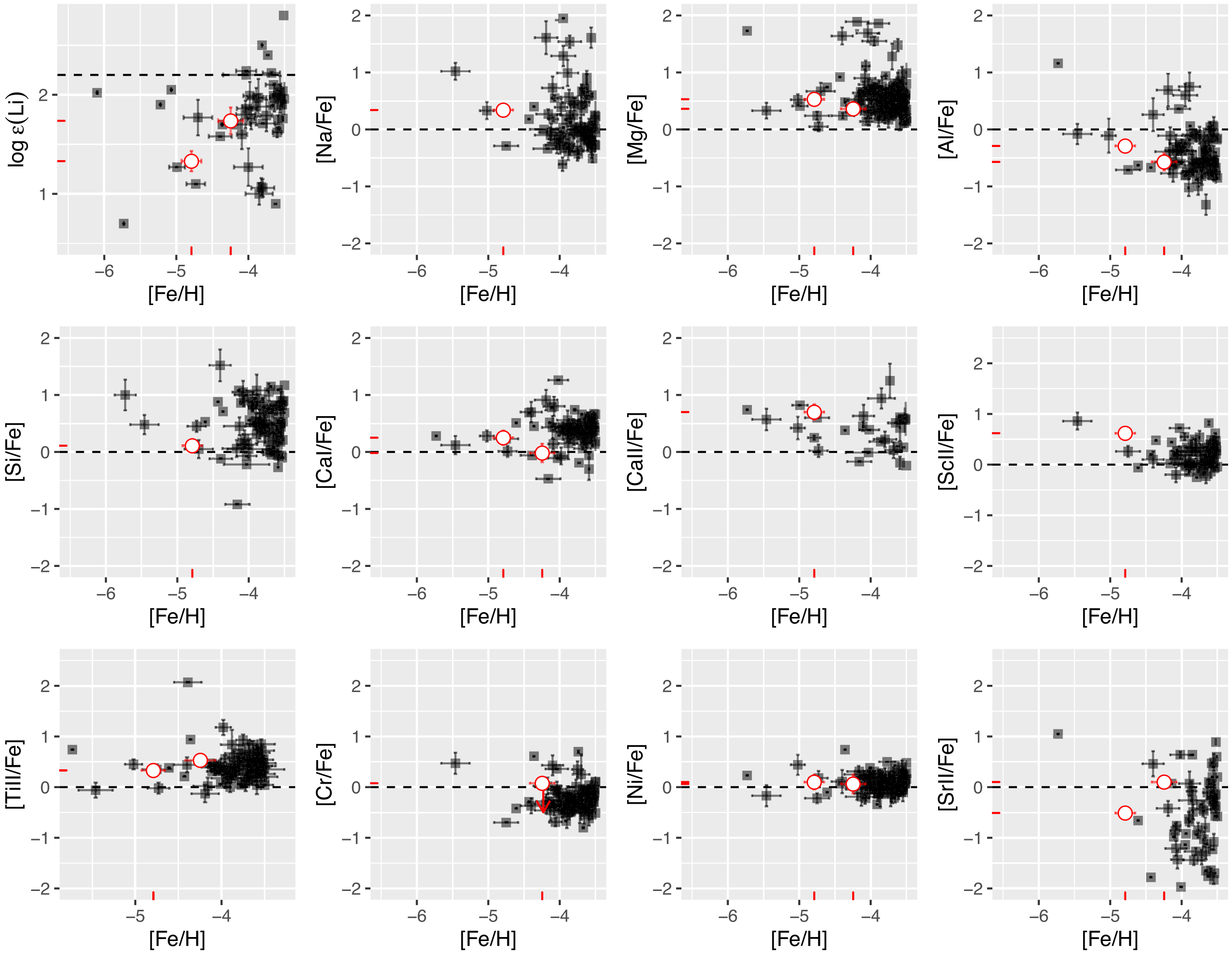

Figure 7. LTE Li abundances (log ε (Li) and [X/Fe] abundance ratios for 11 representative elements in Pr 221 and Pr 237 (shown as red empty symbols) are compared to literature values (black squares).

Our UMP stars Pr 221 and Pr 237 appear to be typical Galactic halo stars with respect to the α-elements Mg, Ca, and Ti, and also Si in Pr 221 (see Fig. 7). Magnesium is enhanced relatively to Fe, with $[\mathrm{Mg/Fe}]_{\mathrm{LTE}} = 0.53$ and 0.26 in Pr 221 and Pr 237, respectively. Slightly lower abundance ratios are derived in NLTE, with $[\mathrm{Mg/Fe}]_{\mathrm{NLTE}} = 0.46$ and 0.24, respectively. In Pr 221, calcium is measured in two ionization stages. The abundance discrepancy found in LTE between Ca I and Ca II nearly disappears in NLTE (see Section 3.6), and we derive a moderate enhancement of Ca ($[\mathrm{Ca\,I/Fe}]_{\mathrm{NLTE}} = 0.14$ and $[\mathrm{Ca\,II/Fe}]_{\mathrm{NLTE}} = 0.24$). For Pr 237, the [Ca/Fe] ratio is around solar, with $[\mathrm{Ca\,I/Fe}]_{\mathrm{LTE}} = -0.06$ and $[\mathrm{Ca\,I/Fe}]_{\mathrm{NLTE}} = -0.09$. Titanium exhibits a substantial overabundance of Ti relatively to Fe in the LTE analysis, with $[\mathrm{Ti/Fe}]_{\mathrm{LTE}} = 0.36$ and 0.56 for Pr 221 and Pr 237, respectively. Since the NLTE corrections for lines of Ti II are smaller than that for lines of Fe I, we obtain lower abundance ratios of $[\mathrm{Ti\,II/Fe}]_{\mathrm{NLTE}} = 0.11$ and 0.38 for Pr 221 and Pr 237, respectively. Thus, in Pr 221, α-enhancement is stronger for Mg than for Si, Ca, and Ti.

Our UMP stars Pr 221 and Pr 237 are not different from the Galactic EMP stars also with respect to Sc, Ni, and probably Cr (see Fig. 7). The scandium abundance was measured for Pr 221 only, from one Sc II line at 4246 Å. We derived a scandium enhancement at the level of $[\mathrm{Sc/Fe}]_{\mathrm{LTE}} = +0.59$. Nickel follows iron. The [Ni/Fe] abundance ratio is expected to be nearly free of the NLTE effects because abundances of both elements were derived from lines of their neutral species, which have probably similar departures from LTE (Mashonkina et al. 2017b). For Cr, we could measure only the upper limit and in one star, Pr 237.

We measure different [Sr/Fe] abundance ratios forfor Pr 221 and Pr 237, with $[\mathrm{Sr/Fe}]_{\mathrm{NLTE}} = -0.72$ ($[\mathrm{Sr/Fe}]_{\mathrm{LTE}} = -0.51$) and -0.04 ($[\mathrm{Sr/Fe}]_{\mathrm{LTE}} = +0.06$), respectively. Again, this is not exceptional for the extremely metal-poor regime of our Galaxy (see Fig. 7). It was not possible to detect spectral features of any other neutron-capture element. Taken together with the measured low [Sr/Fe] ratios, this evidence would indicate that in both stars heavy elements are likely deficient with respect to iron. To clarify this issue, we compared theoretical spectra computed for varying Ba abundance with the observed spectra around the Ba II 4934 Å line. From this comparison, we conclude that if Ba would overabundant relative to Fe at the level $[\mathrm{Ba/Fe}] = +0.5$, we would have observed a clear Ba II absorption line in the UVES spectra of the two targets. Thus, we estimated an upper limit (in LTE) of log ε (Ba) ≤ -2.8 and and ≤ -2.1 for Pr 221 and Pr 237, respectively (Table 3).

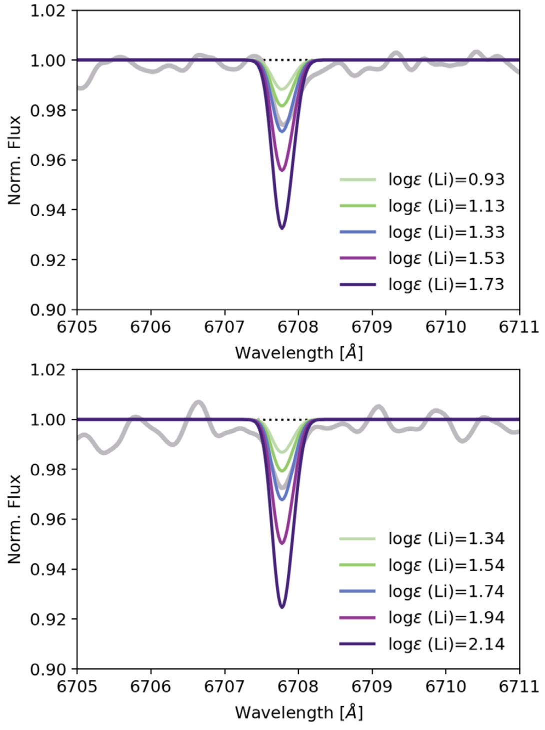

Figure 8. The Li I resonance doublet in Pr 221 (upper panel) and Pr 237 (lower panel) are shown in grey. Theoretical spectra with varying lithium abundance (see the legend) are also shown.

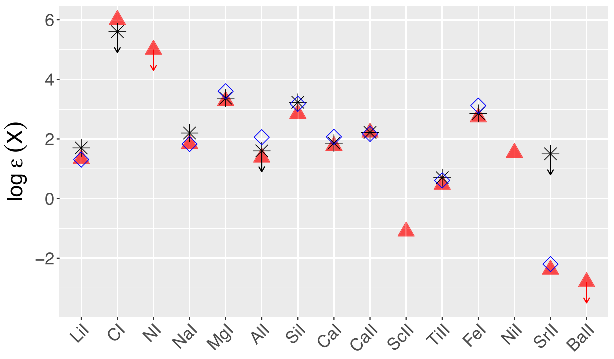

Figure 9. LTE (filled red triangles) and NLTE (empty blue diamonds) abundances derived in this study for Pr 221 are compared with the LTE abundances from Starkenburg et al. (2018) (shown as black asterisks).

4.3 Comparison with previous spectroscopic studies

The abundance of iron determined from Fe I lines in this study agrees with the value published Starkenburg et al. (2018) (log ε (Fe I) = 2.86 ± 0.13) within the measurement errors. Starkenburg et al. (2018) have adopted a $T_{\rm eff} = 5792$ K, which is ∼100 K warmer than the one used here. According to Table 4, the iron abundance from Fe I would increase by ∼0.13 when $T_{\rm eff}$ is raised by 134 K. This is the exact Fe I difference measured in the two analysis. Therefore, we conclude that the difference in the derived iron abundances can entirely be attributed to the stellar parameters adopted in the two studies. Fig. 9 shows that our LTE measurements are generally in line with those presented in Starkenburg et al. (2018) for the elements in common in the two studies (e.g. they are consistent within the uncertainties associated with the measurements).

The higher S/N of the combined UVES spectrum of Pr 221 allows us to also provide measurements for elements for which only upper limits were derived in Starkenburg et al. (2018). From the Al I line at 3961 Å, we derive an LTE abundance of log ε (Al I)$_{\rm LTE}$ = 1.38, which corresponds to log ε (Al I)$_{\rm NLTE}$ = 2.06. This value is in good agreement with the upper limit of log ε (Al I)$_{\rm LTE}$ ≤1.6 measured by Starkenburg et al. (2018). Finally, Starkenburg et al. (2018) provide the upper limit of log ε (Sr II$_{\rm LTE}$ ≤ −1.5 for the fit of the Sr II line at 4077.7 Å. From the same line, we measure an abundance of log ε (Sr II)$_{\rm LTE}$ = −2.38 in LTE, which correspond to log ε (Sr II)$_{\rm NLTE}$ = −2.20 in NLTE. Finally, we present abundances (and upper limits) for nitrogen, scandium, nickel, and barium which were not measured in Starkenburg et al. (2018).

For Pr 237 and the elements in common with Kielty et al. (2021), we observe a perfect agreement between their abundances and our measurements. From the analysis of five Fe I and three Fe II lines, they were able to put an upper limit of [Fe/H] ≤ −4.26, which is consistent with the value we have measured from the analysis of 33 lines ([Fe I/H]$_{\rm LTE}$ = −4.22 ± 0.12). For Li, they measure log ε (Li I) = 1.54 ± 0.20, which is still compatible with the abundance provided by our analysis given the large uncertainty introduced by the continuum placement when fitting the weak Li feature. Kielty et al. (2021) measured log ε (Mg I) = 3.43 ± 0.13, which again agrees with the magnesium abundance of Table 3.

4.4 Model predictions for UMP progenitor SNe

We tentatively assess the properties of the progenitor population of Pr 221 and Pr 237 by comparing their abundances with theoretical model predictions of SN yields from single non-rotating massive Population III stars in the range 9.6–100 M$_{\odot}$ of Heger & Woosley (2010). We use only elements with available NLTE abundances because they are closest to *true* absolute abundances, which are required for a comparison with theoretical predictions. This exercise implicitly assumes that UMP stars are indeed *bona-fide* second-generation objects chemically enriched by a single Pop III SN, as commonly accepted in Galactic archaeology studies.

The model data base includes 120 models and covers a range of explosion energies from 0.3 × 10^{51} to 10 × 10^{51} erg. For each energy, there are models with different (fixed) mixing amounts in the SN ejecta due to Rayleigh–Taylor instabilities (see Heger & Woosley 2010, for further details). We use their publicly available χ^2 matching algorithm to determine which model fits our abundances best.[12] We adopt a similar procedure as the one described in Heger & Woosley (2010), using all available element measurements and upper limits up to atomic number $Z = 30$, as the nucleosynthetic origin of post iron-peak elements in Pop III stars is quite uncertain.

The fitting algorithm treats Sc and Cu as model lower limits because they have multiple different nucleosynthetic pathways (e.g. there are additional production sites not included in the model data) and it ignores Li, Cr, and Zn by default. The same fitting procedure was also used in a number of other studies (e.g. Placco et al. 2015; González Hernández et al. 2020).

Models from Heger & Woosley (2010) reasonably reproduce chemical abundances in both cases. Fitting the abundance pattern of Pr 221 yields a progenitor mass of 14.4 M$_{\odot}$ with little mixing ($f_{\rm mix}$ = 3.98 × 10^{-2}), and a relatively low explosion energy of 1.2 × 10^{51} erg. Similarly, the fitting algorithm returns a low progenitor

---

[12] Accessible at http://starfit.org.

mass (10.6 $M_\odot$) with mixing $f_{\rm mix} = 2.51 \times 10^{-1}$, and a low explosion energy (0.3×10^{51} erg) for Pr 237 as well.

Besides the best-fitting solution, the procedure also provides the ten best model fits ranked by their χ^2 value. If the best-fitting solution is robust, we expect the χ^2 value to rapidly increase between the first- and second-best solutions (Placco et al. 2015). For Pr 221, the first two solutions have the same χ^2 value, but the mass of the progenitor is the same with a slightly different explosion energy (1.2×10^{51} and 0.9×10^{51}erg in the first and second best-fitting solutions, respectively). The progenitor mass returned by the third-best model is only slightly different (14.0 $M_\odot$) with a corresponding variation of the χ^2 value of ∼18 per cent. For Pr 237 , the fitting algorithm returns the same progenitor mass and energies in the first six best-fitting models.

According to Placco et al. (2015), the quality of the match between the abundance pattern of a star to the yields is highly sensitive to the N abundance. In particular, the fitting algorithm predicts a very low N abundances ($[{\rm N/H}] < -6$) where only upper limits on nitrogen are determined. Moreover, carbon and nitrogen abundances are derived using the 1D models, thus they are significantly overestimated compared to those measured in 3D-NLTE model atmospheres (e.g. Norris & Yong 2019, and references therein). To evaluate how changes in the C and N abundances reflect on the progenitor mass we estimated, we ran the matching procedure with both carbon and nitrogen reduced by 1 dex. Overall, we obtain an improvement of the fit. Indeed, the best-fitting model better reproduces carbon abundance, but there is no change in the progenitor model. We also determine the best-fitting parameters after excluding the N abundance from the observed pattern. We found no variations in the progenitor mass or explosion energy in both cases.

To further quantify the uncertainty in progenitor masses computed by the χ^2 matching algorithm and check the parameter degeneracy, we varied NLTE abundances for each star by their uncertainties and run the procedure using the perturbed abundances (see Fraser et al. 2017). To this aim, we assumed that measurements were normally distributed and repeated this perturbation procedure 100 times for each star. The distribution of inferred progenitor masses as a function of the explosion energies, after fitting our perturbed abundance values are shown in Fig. 10. The figure also shows the resulting χ^2 values and the amount of mixing of the different draws.

We find that SN yields for models in a wide range of progenitor masses between 10.10 and 41.00 $M_\odot$ well reproduce the chemical composition of Pr 221. The median value of the progenitor mass is 14.40 $M_\odot$, with a first quartile (Q1) of 14.00 $M_\odot$, a third quartile (Q3) of 30.00 $M_\odot$. In addition to massive progenitors of 20–40 $M_\odot$ exploding in general with low energies ($(1\text{–}2.5) \times 10^{51}$ erg), we also find good fits for progenitors with masses <15 $M_\odot$, with very low explosion energies ($<1 \times 10^{51}$ erg). In particular, we computed a median value for the explosion energy of 1.2×10^{51} erg (Q1 = 0.9×10^{51} and Q3 = 1.8×10^{51} erg), with five notable outliers with explosion energy of 5×10^{51} erg. In general, models with less mixing are favoured, with a median value of $f_{\rm mix} = 0.039\,81$ (Q1 = 0.025 12 and Q3 = 0.063 10). The reduced mixing is likely due to the compact nature of the SN progenitor star in this mass range (Heger & Woosley 2010).

For Pr 237, all the best-fitting models matching its perturbed NLTE abundance pattern have low mass in the range between 9.70 and 15.40 $M_\odot$ (median value of 10.6 $M_\odot$, Q1 = 10.50 $M_\odot$, Q3 = 10.60 $M_\odot$). Also, they have generally experienced low mixing (median value of $f_{\rm mix} = 0.015\,85$, Q1 = 0.015 85, Q3 = 0.081 55) and low explosion energies (median value of 0.3×10^{51} erg, Q1 = 0.3×10^{51} erg, Q3 = 0.6×10^{51} erg). Nine models have progenitor mass of 9.70–9.80 $M_\odot$ and unusually high explosion energy ($>5 \times 10^{51}$ erg). Most probably, the lack of any Na constraint for Pr 237 causes the fit to always prefer lower mass progenitors (Ishigaki et al. 2018).

We illustrate the yields from a selection of well-fitting models in Fig. 11. The models have been selected as those that best match observations for any explosion energy and mixing efficiency within the range of progenitor masses obtained from the 100 simulations for each star. Overall, both Pr 221 and Pr 237 have abundance patterns

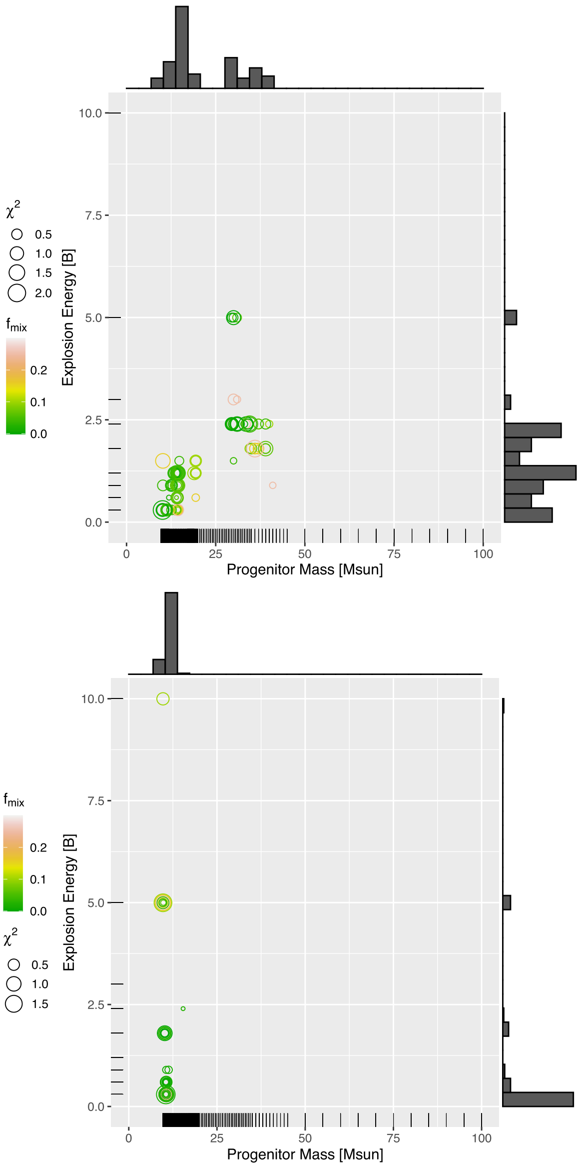

Figure 10. The run of the derived masses versus explosion energies from 100 iterations of the χ^2 matching algorithm using perturbed NLTE abundances are shown for Pr 221 and Pr 237 in the top and bottom panel, respectively. Data points are colour-coded according to the amount of mixing characterizing the best-fitting model. The size of the data points is a function of the derived χ^2 value. Marginal histograms for the progenitor mass and explosion energy are shown as well. The rug plots display the grid of masses and explosion energies from Heger & Woosley (2010). There are 126 different masses in the range 9.6–100 $M_\odot$. Model stars differ by only 0.1–0.2 $M_\odot$ toward the lighter end of the mass range explored in Heger & Woosley (2010) to take into account for their different pre-SN properties (see Heger & Woosley 2010).

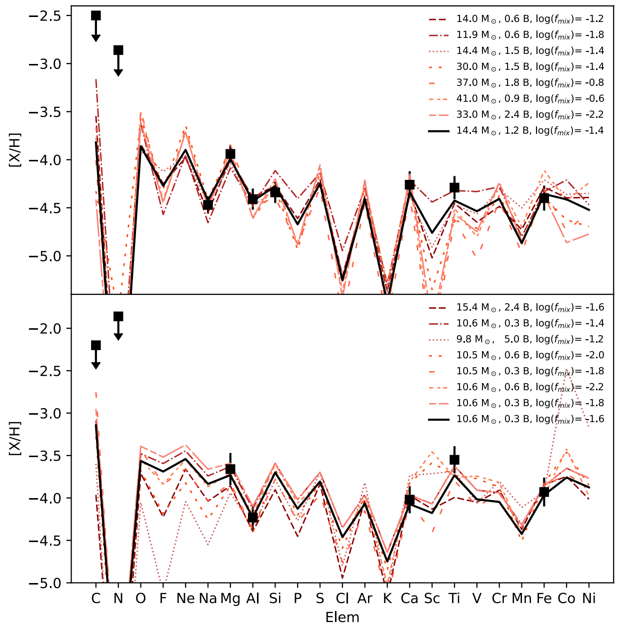

Figure 11. SN model yields assuming a selection of different progenitor mass, explosion energy, and mixing that best match the NLTE abundance patterns of Pr 221 and Pr 237 (black squares) are shown in the top and bottom panel, respectively. The best-fitting model is plotted as a continuous black line.

have NLTE elemental abundance patterns that are well reproduced by the SN models of Heger & Woosley (2010).

As discussed above, the existence of a nitrogen measurement is fairly important for the model fit procedure (e.g. Placco et al. 2015). Indeed, in their study of 21 UMP stars observed at high-resolution, Placco et al. (2015) found that stars with upper limits on nitrogen have progenitor masses in the 10.6–15.0 M$_\odot$ range. In contrast, progenitor masses for stars with actual nitrogen measurements show a bimodal distribution toward higher masses (e.g. progenitor masses in the range 20.5–23.0 and 27.0–28.0 M$_\odot$). Thus, we caveat that the lack of nitrogen abundance measurements is possibly affecting the progenitor mass determination.

Finally, the measured abundance ratios for [Na/Mg], [Al/Mg], as well as [Ca/Mg] rule out any contamination from massive ($140 < M < 260\,\mathrm{M}_\odot$) exploding as pair-instability supernovae (PISNe; Heger & Woosley 2002) for both stars. In particular, the PISN models predict low [(Na,Al)/Mg] and high [Ca/Mg] abundance ratios ([Na/Mg] = −1.5, [Al/Mg] = −1.20, and [Ca/Mg] ∼ 0.5–1.3; Takahashi, Yoshida & Umeda 2018) that are not observed in the analysed stars.[13]

.

5 CONCLUSIONS

We have presented a high-resolution spectroscopic follow-up of two UMP stars identified in the *Pristine* photometry and previously analysed in Starkenburg et al. (2018) (Pr 221) and Aguado et al. (2019a) (Pr 237) based on the medium-resolution spectrum and in Kielty et al. (2021) (Pr 237) based on the high-resolution spectrum. We now briefly summarize our findings:

(i) We found that neither star shows any significant RV variations during the observations in 2018 August (four nights; Starkenburg et al. 2018)/2018 June (two nights; Kielty et al. 2021) – for Pr 221 and Pr 237, respectively – or those in 2020 (six nights; this paper), or between the two investigations.

(ii) We confirm the UMP nature of both stars, with measured Fe abundances of $[\mathrm{Fe/H}]_{\mathrm{LTE}} = -4.79 \pm 0.14$ and -4.22 ± 0.12 for Pr 221 and Pr 237, respectively. This translates to $[\mathrm{Fe/H}]_{\mathrm{NLTE}} = -4.38 \pm 0.13$ and -3.93 ± 0.12 when departures from LTE are taken into account.

(iii) The upper limits we derive on the C abundances are compatible with the two stars having a moderate C overabundance. In particular, the upper limit and tentative measurement for Pr 221 we derive in Section 4.1 using constraints from Al features lies on the border of the carbon-normal stars. We were able also to put an upper limit to the N abundance of both objects from the analysis of the NH feature at ∼3360 Å.

(iv) Measured abundances for Li, Na, Mg, Al, Si, Ca, Sc, Cr, Ti, and Ni in general exhibit good agreement with those of Galactic EMP and UMP stars. Li is depleted in Pr 221 probably because of its low effective temperature. On the other hand, the low Li abundance of Pr 237 is intrinsic as observed in many unevolved stars with $[\mathrm{Fe/H}] < -3.5$ (Bonifacio et al. 2018). We measure different [Sr/Fe] abundance ratios for Pr 221 and Pr 237, with $[\mathrm{Sr\,II/Fe}]_{\mathrm{LTE}} = -0.51$ ($[\mathrm{Sr\,II/Fe}]_{\mathrm{NLTE}} = -0.72$) and $+0.06$ ($[\mathrm{Sr\,II/Fe}]_{\mathrm{NLTE}} = -0.05$), respectively. The low [Sr II/Fe] abundance ratios together with the absence of any other heavier element features supports the interpretation of Bonifacio et al. (2015) that stars belonging to the low-carbon-band are carbon enhanced metal-poor stars with no overabundances of neutron-capture elements (CEMP-no according to the classification of Beers & Christlieb 2005) as opposed to stars on the high-carbon-band in which the high carbon abundance is the consequence of mass-transfer in a binary system from companion in its asymptotic giant branch phase (e.g. Hansen et al. 2016; Yoon et al. 2016; but see also Arentsen et al. 2019 for a discussion on the rôle of binarity in shaping the abundance pattern of CEMP-no stars). No detection of any RV variation further supports such scenario.

(v) Under the assumption that the chemical pattern of the two UMP stars directly reflect the composition of the parent gas cloud (e.g. stars have been enriched by a single Pop III SN), their NLTE abundances suggest in both cases low-energy SN progenitors with masses from 10.6 to 14.4 M$_\odot$ and energies in the range (0.3–1.2) × 10^{51} erg.

Ultra-metal-poor stars are rare relics of the first stages of star formation and cosmic evolution (Beers & Christlieb 2005). As such, they guide our understanding on the first nucleosynthesis events and the first Pop III stars (Bromm 2013), the earliest phases of chemical enrichment (Frebel & Norris 2015), as well as the formation of the first Pop II stars with low mass (Frebel et al. 2007; Klessen, Glover & Clark 2012; Chiaki, Tominaga & Nozawa 2017).

Obtaining reliable data for a significant sample of them is crucial to undertake large and systematic investigations of this important stellar population. Unfortunately,although the number of known UMP stars has greatly increased over the last years (e.g. Beers et al. 1985, 1992; Norris, Bessell & Pickles 1985; Anthony-Twarog et al. 1991, 2000; Schuster et al. 1996; Allende Prieto et al. 2000; Christlieb 2003; Keller et al. 2007; Schlaufman & Casey 2014; Meléndez et al. 2016; Starkenburg et al. 2017; Placco et al. 2019), the relatively small number currently available still precludes any full stellar

---

[13] We measure for Pr 221 [Na/Mg] = −0.53, [Al/Mg] = −0.47, and [Ca/Mg] = −0.32. The derived [Al/Mg] and [Ca/Mg] abundance ratios for Pr 237are [Al/Mg] = −0.54 and [Ca/Mg] = −0.33.

population analysis. In the near future, ongoing synergies between large photometric and spectroscopic surveys will revolutionize the field, yielding extremely large samples of stars with [Fe/H] < -3.0 and delivering additional UMP stars.

ACKNOWLEDGEMENTS

CL acknowledges funding from Ministero dell'Università e della Ricerca (MIUR) through the Programme 'Rita Levi Montalcini' (grant PGR18YRML1). JIGH acknowledges financial support from the Spanish Ministry of Science and Innovation (MICINN) project AYA2017-86389-P, and also from the Spanish MICINN under 2013 Ramón y Cajal program RYC-2013-14875. NM, EC, PB, VH, and GK gratefully acknowledge support from the French National Research Agency (ANR) funded projects 'Pristine' (ANR-18-CE31-0017). AA and NFM acknowledge funding from the European Research Council (ERC) under the European Unions Horizon 2020 research and innovation programme (grant agreement No. 834148). ES acknowledges funding through VIDI grant 'Pushing Galactic Archaeology to its limits' (with project number VI.Vidi.193.093), which is funded by the Dutch Research Council (NWO). The authors thank the International Space Science Institute, Berne, Switzerland for providing financial support and meeting facilities to the international team 'Pristine'.

This paper is based on observations collected at the European Organisation for Astronomical Research in the Southern Hemisphere and observations made with the Gran Telescopio de Canarias, operated by the GRANTECAN team at the Observatorio del Roque de los Muchachos, La Palma, Spain, of the Instituto de Astrofísica de Canarias. This work has made use of data from the European Space Agency (ESA) mission *Gaia* (https://www.cosmos.esa.int/gaia), processed by the *Gaia* Data Processing and Analysis Consortium (DPAC; https://www.cosmos.esa.int/web/gaia/dpac/consortium). Funding for the DPAC has been provided by national institutions, in particular the institutions participating in the *Gaia* Multilateral Agreement.

This paper is based on observations collected at the European Southern Observatory under ESO programmes 299.D-5042, 102.D-0766, and 104.B-0305 and on observations made with the Gran Telescopio Canarias (GTC), installed at the Spanish Observatorio del Roque de los Muchachos of the Instituto de Astrofísica de Canarias, in the island of La Palma. Programme ID 39-GTC16/17A.

DATA AVAILABILITY

The data underlying this paper will be shared on reasonable request to the corresponding author.

REFERENCES

, , , ,
Abate C., Pols O. R., Izzard R. G., Karakas A. I., 2015, A&A, 581, A22
Aguado D. S. et al., 2019a, MNRAS, 490, 2241
Aguado D. S., Allende Prieto C., González Hernández J. I., Rebolo R., 2018b, ApJ, 854, L34
Aguado D. S., Allende Prieto C., González Hernández J. I., Rebolo R., Caffau E., 2017a, A&A, 604, A9
Aguado D. S., González Hernández J. I., Allende Prieto C., Rebolo R., 2017b, A&A, 605, A40
Aguado D. S., González Hernández J. I., Allende Prieto C., Rebolo R., 2018a, ApJ, 852, L20
Aguado D. S., González Hernández J. I., Allende Prieto C., Rebolo R., 2019b, ApJ, 874, L21
Albareti F. D. et al., 2017, ApJS, 233, 25
Aldenius M., Tanner J. D., Johansson S., Lundberg H., Ryan S. G., 2007, A&A, 461, 767
Alexeeva S., Pakhomov Y., Mashonkina L., 2014, Astron. Lett., 40, 406
Allende Prieto C. et al., 2015, A&A, 579, A98
Allende Prieto C., Beers T. C., Wilhelm R., Newberg H. J., Rockosi C. M., Yanny B., Lee Y. S., 2006, ApJ, 636, 804
Allende Prieto C., Rebolo R., García López R. J., Serra-Ricart M., Beers T. C., Rossi S., Bonifacio P., Molaro P., 2000, AJ, 120, 1516
Andrae R. et al., 2018, A&A, 616, A8
Andrievsky S. M., Spite M., Korotin S. A., Spite F., Bonifacio P., Cayrel R., Hill V., François P., 2007, A&A, 464, 1081
Anthony-Twarog B. J., Laird J. B., Payne D., Twarog B. A., 1991, AJ, 101, 1902
Anthony-Twarog B. J., Sarajedini A., Twarog B. A., Beers T. C., 2000, AJ, 119, 2882
Arentsen A. et al., 2020, MNRAS, 496, 4964
Arentsen A., Starkenburg E., Shetrone M. D., Venn K. A., Depagne É., McConnachie A. W., 2019, A&A, 621, A108
Arpigny C., Magain P., 1983, A&A, 127, L7
Asplund M., 2005, ARA&A, 43, 481
Asplund M., García Pérez A. E., 2001, A&A, 372, 601
Barklem P. S., Belyaev A. K., Dickinson A. S., Gadéa F. X., 2010, A&A, 519, A20
Barklem P. S., Belyaev A. K., Spielfiedel A., Guitou M., Feautrier N., 2012, A&A, 541, A80
Baumueller D., Butler K., Gehren T., 1998, A&A, 338, 637
Baumueller D., Gehren T., 1996, A&A, 307, 961
Baumueller D., Gehren T., 1997, A&A, 325, 1088
Beers T. C., Christlieb N., 2005, ARA&A, 43, 531
Beers T. C., Preston G. W., Shectman S. A., 1985, AJ, 90, 2089
Beers T. C., Preston G. W., Shectman S. A., 1992, AJ, 103, 1987
Belyaev A. K., 2013, A&A, 560, A60
Belyaev A. K., Voronov Y. V., Yakovleva S. A., Mitrushchenkov A., Guitou M., Feautrier N., 2017, ApJ, 851, 59
Belyaev A. K., Yakovleva S. A., Barklem P. S., 2014, A&A, 572, A103
Belyakova E. V., Mashonkina L. I., 1997, Astron. Rep., 41, 530
Bonifacio P. et al., 2009, A&A, 501, 519
Bonifacio P. et al., 2015, A&A, 579, A28
Bonifacio P. et al., 2018, A&A, 612, A65
Bonifacio P. et al., 2019, MNRAS, 487, 3797
Bromm V., 2013, Rep. Prog. Phys., 76, 112901
Butler K., Giddings J., 1985, Newsletter on the Analysis of Astronomical Spectra, No. 9. University of London
Caffau E. et al., 2011, Nature, 477, 67
Caffau E. et al., 2012, A&A, 542, A51
Caffau E. et al., 2016, A&A, 595, L6
Caffau E. et al., 2017, Astron. Nachr., 338, 686
Caffau E. et al., 2020, MNRAS, 493, 4677
Castelli F., Kurucz R. L., 2003, in Piskunov N., Weiss W. W., Gray D. F., eds, Proc. IAU Symp. 210, Modelling of Stellar Atmospheres. Kluwer, Dordrecht, p. A20
Cenarro A. J. et al., 2019, A&A, 622, A176
Chiaki G., Tominaga N., Nozawa T., 2017, MNRAS, 472, L115
Chiappini C., Ekström S., Meynet G., Hirschi R., Maeder A., Charbonnel C., 2008, A&A, 479, L9
Choplin A., Hirschi R., Meynet G., Ekström S., Chiappini C., Laird A., 2018, A&A, 618, A133
Choplin A., Maeder A., Meynet G., Chiappini C., 2016, A&A, 593, A36
Choplin A., Siess L., Goriely S., 2021, A&A, 648, A119
Christlieb N. et al., 2002, Nature, 419, 904
Christlieb N., 2003, Rev. Mod. Astron., 16, 191
Christlieb N., Gustafsson B., Korn A. J., Barklem P. S., Beers T. C., Bessell M. S., Karlsson T., Mizuno-Wiedner M., 2004, ApJ, 603, 708
Christlieb N., Schörck T., Frebel A., Beers T. C., Wisotzki L., Reimers D., 2008, A&A, 484, 721
Collet R., Asplund M., Trampedach R., 2007, A&A, 469, 687

Collet R., Nordlund, Å., Asplund M., Hayek W., Trampedach R., 2018, MNRAS, 475, 3369

Dekker H., D'Odorico S., Kaufer A., Delabre B., Kotzlowski H., 2000, in Iye M., Moorwood A. F., eds, Proc. SPIE Conf. Ser. Vol. 4008, Optical and IR Telescope Instrumentation and Detectors. SPIE, Bellingham, p. 534

Dotter A., 2016, ApJS, 222, 8

Ekström S., Meynet G., Chiappini C., Hirschi R., Maeder A., 2008, A&A, 489, 685

Fraser M., Casey A. R., Gilmore G., Heger A., Chan C., 2017, MNRAS, 468, 418

Frebel A. et al., 2005, Nature, 434, 871

Frebel A. et al., 2006, ApJ, 652, 1585

Frebel A., Collet R., Eriksson K., Christlieb N., Aoki W., 2008, ApJ, 684, 588

Frebel A., Johnson J. L., Bromm V., 2007, MNRAS, 380, L40

Frebel A., Norris J. E., 2015, ARA&A, 53, 631

Fulbright J. P. et al., 2010, ApJ, 724, L104

Gaia Collaboration et al., 2016, A&A, 595, A1

Gaia Collaboration et al., 2018, A&A, 616, A1

Gallagher A. J., Caffau E., Bonifacio P., Ludwig H. G., Steffen M., Homeier D., Plez B., 2017, A&A, 598, L10

Gallagher A. J., Caffau E., Bonifacio P., Ludwig H. G., Steffen M., Spite M., 2016, A&A, 593, A48

Gehren T., Liang Y. C., Shi J. R., Zhang H. W., Zhao G., 2004, A&A, 413, 1045

González Hernández J. I., Aguado D. S., Allende Prieto C., Burgasser A. J., Rebolo R., 2020, ApJ, 889, L13

González Hernández J. I., Bonifacio P., 2009, A&A, 497, 497

González Hernández J. I., Bonifacio P., Caffau E., Ludwig H. G., Steffen M., Monaco L., Cayrel R., 2019, A&A, 628, A111

González Hernández J. I., Bonifacio P., Ludwig H. G., Caffau E., Behara N. T., Freytag B., 2010, A&A, 519, A46

Hansen T. et al., 2014, ApJ, 787, 162

Hansen T. T., Andersen J., Nordström B., Beers T. C., Placco V. M., Yoon J., Buchhave L. A., 2016, A&A, 586, A160

Hansen T. T., Andersen J., Nordström B., Beers T. C., Yoon J., Buchhave L. A., 2015, A&A, 583, A49

Heger A., Woosley S. E., 2002, ApJ, 567, 532

Heger A., Woosley S. E., 2010, ApJ, 724, 341

Henden A. A., Templeton M., Terrell D., Smith T. C., Levine S., Welch D., 2015, American Astronomical Society Meeting Abstracts #225, 336.16

Ishigaki M. N., Tominaga N., Kobayashi C., Nomoto K., 2018, ApJ, 857, 46

Keller S. C. et al., 2007, Publ. Astron. Soc. Aust., 24, 1

Keller S. C. et al., 2014, Nature, 506, 463

Kielty C. L. et al., 2021, MNRAS, 506, 1438

Klessen R. S., Glover S. C. O., Clark P. C., 2012, MNRAS, 421, 3217

Koesterke L., Allende Prieto C., Lambert D. L., 2008, ApJ, 680, 764

Komiya Y., Suda T., Yamada S., Fujimoto M. Y., 2020, ApJ, 890, 66

Kurucz R. L., 2005, Mem. Soc. Astron. Ital. Suppl., 8, 14

Lawrence A. et al., 2007, MNRAS, 379, 1599

Lind K., Asplund M., Barklem P. S., 2009, A&A, 503, 541

Lodders K., Palme H., Gail H. P., 2009, Solar System, Landolt-Börnstein – Group VI Astronomy and Astrophysics, Vol. 4B, Springer-Verlag Berlin Heidelberg, p. 712

Maeder A., Meynet G., Chiappini C., 2015, A&A, 576, A56

Mashonkina L. I., Belyaev A. K., Shi J.-R., 2016, Astron. Lett., 42, 366

Mashonkina L., 2013, A&A, 550, A28

Mashonkina L., 2020, MNRAS, 493, 6095

Mashonkina L., 2021, MNRAS, 0, 0

Mashonkina L., Gehren T., Shi J.-R., Korn A. J., Grupp F., 2011, A&A, 528, A87

Mashonkina L., Jablonka P., Sitnova T., Pakhomov Y., North P., 2017b, A&A, 608, A89

Mashonkina L., Korn A. J., Przybilla N., 2007, A&A, 461, 261

Mashonkina L., Sitnova T., Belyaev A. K., 2017a, A&A, 605, A53

Masseron T. et al., 2014, A&A, 571, A47

Meléndez J., Placco V. M., Tucci-Maia M., Ramírez I., Li T. S., Perez G., 2016, A&A, 585, L5

Mendes de Oliveira C. et al., 2019, MNRAS, 489, 241

Mészáros S. et al., 2012, AJ, 144, 120

Meynet G., Ekström S., Maeder A., 2006, A&A, 447, 623

Mucciarelli A., 2013, preprint (arXiv:1311.1403)

Mucciarelli A., 2017, Astrophysics Source Code Library, record ascl:1708.020

Mucciarelli A., Bellazzini M., 2020, Res. Notes AAS, 4, 52

Mucciarelli A., Pancino E., Lovisi L., Ferraro F. R., Lapenna E., 2013, ApJ, 766, 78

Nomoto K., Kobayashi C., Tominaga N., 2013, ARA&A, 51, 457

Nordlander T., Amarsi A. M., Lind K., Asplund M., Barklem P. S., Casey A. R., Collet R., Leenaarts J., 2017, A&A, 597, A6

Norris J. E. et al., 2013, ApJ, 762, 28

Norris J. E., Christlieb N., Bessell M. S., Asplund M., Eriksson K., Korn A. J., 2012, ApJ, 753, 150

Norris J. E., Christlieb N., Korn A. J., Eriksson K., Bessell M. S., Beers T. C., Wisotzki L., Reimers D., 2007, ApJ, 670, 774

Norris J. E., Yong D., 2019, ApJ, 879, 37

Norris J., Bessell M. S., Pickles A. J., 1985, ApJS, 58, 463

Paxton B., Bildsten L., Dotter A., Herwig F., Lesaffre P., Timmes F., 2011, ApJS, 192, 3

Placco V. M. et al., 2019, ApJ, 870, 122

Placco V. M., Frebel A., Beers T. C., Stancliffe R. J., 2014, ApJ, 797, 21

Placco V. M., Frebel A., Lee Y. S., Jacobson H. R., Beers T. C., Pena J. M., Chan C., Heger A., 2015, ApJ, 809, 136

Rasmussen K. C. et al., 2020, ApJ, 905, 20

Sakari C. M. et al., 2018, ApJ, 868, 110

Samland M., 1998, ApJ, 496, 155

Sbordone L. et al., 2010, A&A, 522, A26

Sbordone L., 2005, Mem. Soc. Astron. Ital. Suppl., 8, 61

Schlafly E. F., Finkbeiner D. P., 2011, ApJ, 737, 103

Schlaufman K. C., Casey A. R., 2014, ApJ, 797, 13

Schlegel D. J., Finkbeiner D. P., Davis M., 1998, ApJ, 500, 525

Schuster W. J., Nissen P. E., Parrao L., Beers T. C., Overgaard L. P., 1996, A&AS, 117, 317

Sestito F. et al., 2019, MNRAS, 484, 2166

Sestito F. et al., 2020, MNRAS, 497, L7

Sitnova T. M., Mashonkina L. I., Ryabchikova T. A., 2016, MNRAS, 461, 1000

Skrutskie M. F. et al., 2006, AJ, 131, 1163

Spite F., Spite M., 1982a, A&A, 115, 357

Spite M., Caffau E., Bonifacio P., Spite F., Ludwig H. G., Plez B., Christlieb N., 2013, A&A, 552, A107

Spite M., Spite F., 1982b, Nature, 297, 483

Starkenburg E. et al., 2017, MNRAS, 471, 2587

Starkenburg E. et al., 2018, MNRAS, 481, 3838

Starkenburg E., Shetrone M. D., McConnachie A. W., Venn K. A., 2014, MNRAS, 441, 1217

Steenbock W., Holweger H., 1984, A&A, 130, 319

Steinmetz M. et al., 2006, AJ, 132, 1645

Stetson P. B., Pancino E., 2008, PASP, 120, 1332

Takahashi K., Yoshida T., Umeda H., 2018, ApJ, 857, 111

Tominaga N., Iwamoto N., Nomoto K., 2014, ApJ, 785, 98

Umeda H., Nomoto K., 2003, Nature, 422, 871

Venn K. A. et al., 2020, MNRAS, 492, 3241

Whitten D. D. et al., 2021, ApJ, 912, 147

Wolf C. et al., 2018, Publ. Astron. Soc. Aust., 35, e010

Yan Z.-C., Drake G. W. F., 1995, Phys. Rev. A, 52, 3711

Yoon J. et al., 2016, ApJ, 833, 20

Yoon J. et al., 2018, ApJ, 861, 146

Youakim K. et al., 2017, MNRAS, 472, 2963

This paper has been typeset from a TEX/LATEX file prepared by the author.